2018

Online condition monitoring and fault detection in induction motor bearings

Sengoz, Turker

Online Condition Monitoring and Fault Detection in Induction Motor Bearings

by

Turker Sengoz

A thesis presented to the Lakehead University in fulfillment of the thesis requirements for the degree of Master of Science in Mechanical Engineering

Lakehead University, Thunder Bay, Ontario, Canada

Abstract

Induction motors (IMs) are commonly used in industry. Online IM health condition monitoring aims to recognize motor defect at its early stage to prevent motor performance degradation and reduce maintenance costs. The most common fault in IMs is related to bearing defects. Although many signal processing techniques have been proposed in literature for bearing fault detection using vibration and stator current signals, reliable bearing fault diagnosis still remains a challenging task. One of the reasons is that a rolling element bearing is not a simple component, but a system; its related features could be time-varying and nonlinear in nature. The objective of this study is to investigate an online condition monitoring system for IM bearing fault detection. The monitoring system consists of two main modules: smart data acquisition (DAQ) and bearing fault detection. In this work, a smart current sensor system is developed for data acquisition wirelessly. The DAQ system is tested for wireless data transmission, consistent data sampling, and low power consumption. The data acquisition operation is controlled by using an adaptive interface. In bearing fault detection, a generalized Teager-Kaiser energy (GTKE) technique is proposed for nonlinear bearing feature extraction and fault detection using both vibration and current signals. The proposed GTKE technique will demodulate the signal by tracking the instantaneous signal energy. An optimization method is proposed to enhance the fault-related features and improve signal-to-noise ratio. The effectiveness of the proposed technique is verified experimentally using a series of IM tests. The robustness is examined under different operating conditions.

Acknowledgments

First and foremost, I am very grateful to my Supervisor, Dr. Wilson Wang for his academic guidance, patience, constant support, encouragement and giving me the opportunity to work in this beautiful country. I consider myself lucky to work with such a wise professor, in such a motivating research environment where the students are always treated with utmost respect.

I will always remember the support of my research colleagues and my dearest friends Peter and Rahul for their many helpful suggestions.

I would like to thank Dr. Yushi Zhou and Dr. Jian Deng for their reviewing comments and helpful feedback.

My sincerest gratitude to my friends back home, Berkcan, Ege, Semkan, Ozgun, and many good friends I have met here in Canada.

Last but not least, I will be forever indebted and grateful to my lovely parents, Mrs. Elif & Mr. Tamer Şengöz and my brother Cenker, who supported me throughout my studies and were always there for me.

Dedication

Anneme, babama ve ağabeyime…

To my mother, my father, and my brother...

Table of Contents

List of Figures

xiii

List of Tables

List of Abbreviations

ADC   Analog-to-digital converter

AM   Amplitude modulation

CLK   Clock-select

CS   Chip-select

CM   Condition monitoring

CPU   Central processing unit

CTC   Clear timer on compare

DAQ   Data-acquisition

EPROM   Erasable programmable read-only memory

FFT   Fast Fourier transform

FT   Fourier Transform

GTKE   Generalized Teager-Kaiser energy

I2C   Inter-integrated circuit

IC   Integrated circuit

IM   Induction motor

MCU   Micro-controller

MISO   Master-in-slave-out

MOSI   Master-out-slave-in

MCSA	Motor current signature analysis
RAM	Random access memory
RF	Radio frequency
ROM	Read-only memory
SNR	Signal-to-noise ratio
SPI	Serial peripheral interface
SRAM	Static random-access memory
TKE	Teager-Kaiser energy
WDT	Watchdog timer
WSS	Wireless smart sensor
WT	Wavelet transform

Chapter 1 Introduction

1.1 Overview

Condition monitoring (CM) is a maintenance strategy to track the health state of machinery. The purpose is to recognize machinery a defect at its earliest stage so as to prevent machinery performance degradation and malfunction, and to assist schedule repair and maintenance operations. Reliable health monitoring information of critical machinery can reduce costs by preventing downtime due to unexpected catastrophic failures and improving equipment reliability [1]. Figure 1.1 illustrates the CM process. The appropriate signals representing the machine health condition are collected using data acquisition (DAQ) systems. DAQ system consists of transducers/sensors, signal conditioning and an analog-to-digital converter (ADC), etc. The fault-related features contained in the collected signals are extracted using appropriate signal processing techniques. The fault diagnostics is carried out by decision making. Traditionally, decision making is done by categorizing features into different categories corresponding different machinery health conditions. This study focuses on the DAQ and feature extraction of a CM system.
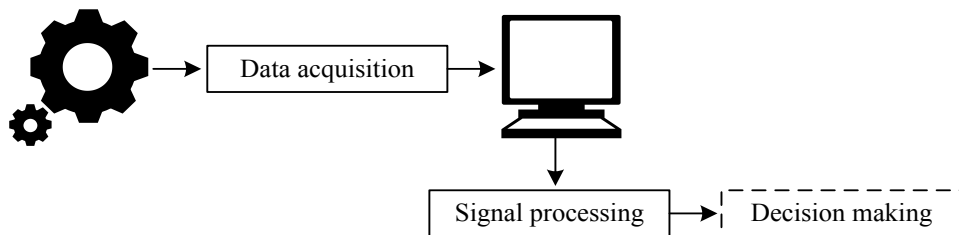
Figure 1.1. A flowchart of a machinery CM system.

Traditional CM is implemented by offline data collection where the signal is measured manually by field technicians. In an online CM system, the DAQ system is remotely activated. Remotely operating the DAQ system allows data collection from machinery from hazardous locations without endangering the safety of the personnel. Furthermore, with a remote-controlled DAQ system, it is feasible to collect data in a controlled mode and on a continuous basis. The installation cost can also be reduced by using wireless sensor networks [2]. Moreover, with the

decreasing transducer and microcontroller unit (MCU) costs, it is possible to use of smart sensor technologies with onboard DAQ systems and wireless communication modules [3].

Induction motors (IMs) are commonly used in different industrial applications, such as manufacturing facilities, electric vehicles, and pump stations. IMs are the workhorse of the industry due to their easy installation, durability, and low maintenance requirements. An IM is a machine that converts electrical energy into mechanical energy. In general, IMs power consumption can reach up to 50% of the generated electricity [4]. Due to these facts, it is of great importance to monitor the health of the IMs with reliable fault diagnostic methods to prevent performance degradation, minimize shutdown times and reduce maintenance costs [5].

Figure 1.2 shows the cutaway view of an IM. A general IM is composed of stator windings, a rotor, two rolling element bearings and the output shaft. These components operate under a combination of thermal, mechanical, electrical and environmental stresses [6]. These stresses lead to defects in IMs such as mechanical faults (e.g., broken rotor bar, shaft misalignment, bearing damage) and electrical faults (e.g., unbalanced supply voltage, winding short-circuits, grounding faults) [7]. Surveys indicate that among these, bearing defects constitute up to 70% of the faults in small to medium sized IMs [8, 9]. Bearings frequently fail due to dynamic loading in operation [10, 11]. A damaged bearing generates not only extra vibration and noise, but also extra heat due to the increased friction in the defected location, which in turn decreases the lifetime of the IM.
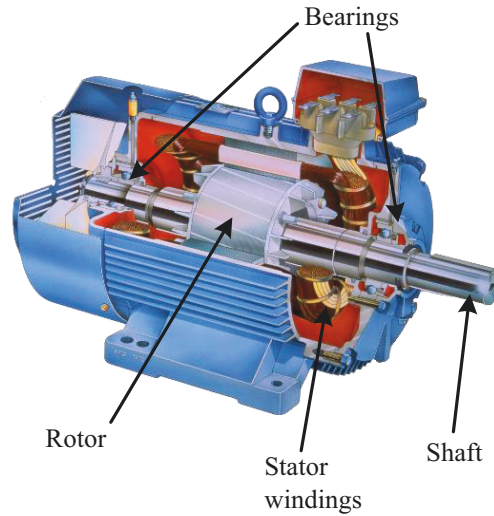
Figure 1.2. Cutaway view of an IM (reproduced from [12]).

Bearing faults are classified as distributed faults (e.g., wear, roughness) and localized fatigue defects (e.g., pits, crack) [13]. In general, distributed bearing faults originate from a localized defect such as a small pit or a spall [14]. This work will focus on IM fault diagnosis for localized bearing defects, using a wireless smart sensor (WSS) DAQ system.

1.2 Literature Review

Through this literature review, the related work on the smart sensor DAQ systems and bearing fault detection techniques are investigated.

1.2.1 Smart Sensors

A sensor is a device to transform a specific energy to the electrical signal. These energy forms include chemical, radiant, mechanical, magnetic, thermal and electrical types [15]. A sensor typically consists of a transducer that takes the input from the physical environment and a transmitter that outputs an electrical signal (e.g., voltage, current). A classical sensor requires an external DAQ unit that can provide the power supply to the sensor, to sample the analog output of the sensor into digital values and to perform signal pre-conditioning such as anti-aliasing,

offsetting and amplification. In comparison, a smart sensor is a device that integrates the sensor with an onboard DAQ system as well as the communication capabilities for ADC and data transmission [16]. The first commercial smart sensor device was an air data transducer developed by Honeywell in 1984 for aerospace applications [17]. Since then, the smart sensor technologies have been implemented in many intelligent monitoring and control applications [18].

Figure 1.3 demonstrates a smart sensor setup with each module serving a specific function in the overall operation. The signal of interest is converted to an electrical signal by the sensor. The output signal of many analog sensors requires signal conditioning before the signal is digitized. The signal conditioning unit ensures the output signal of the sensor is suitable for transmission, display, and recording [19]. The MCU is the unit that contains the processor unit, system clock, embedded memory, input/output pins, ADC or digital-to-analog converter. The functions of an MCU in a smart sensor are to set the voltage reference of the sensors, operate the ADC to convert the analog voltage to digital values, store, and process data and transmit the results for further processing. The communication interface is responsible for data transmission between the smart sensor and other devices such as a computer or another MCU. A communication can be wired using serial communication protocols or wireless using a transceiver. MCUs are often compact low-power devices that can be battery-powered. Some researchers have studied the effectiveness of the MCU-based low-cost smart sensors as DAQ units [20, 21].

Signal →	Sensor	Signal conditioning	Microcontroller	ADC	Communication interface
	Power source				
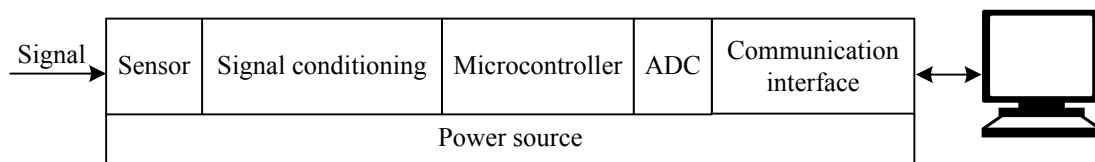
Figure 1.3. A block diagram of a typical smart sensor with an onboard DAQ unit.

The CM using wired DAQ has been employed in the industry [22]. However, wired CM has limitations in real industrial applications, such as expensive installation and maintenance costs due to the additional cabling, labor, hardware and labor, as well as limitations due to constrained space. WSSs provide an alternative cost-effective mobile monitoring solution for fault diagnostics.

A WSS transmits the data to a receiver device using wireless communication, such as radio frequency (RF) transmission, ZigBee, or wi-fi.

To design a WSS system for remote CM, specific requirements to be considered include higher sampling frequency rates and sufficient ADC resolution. A reliable wireless DAQ should prevent any loss of communication packets in transmission. The challenge in the WSS is related to the development of a reliable DAQ system and the selection of suitable wireless communication protocols that meet the requirements of the CM with optimal use of the limited resources, such as memory, processor speed, and battery power.

1.2.2 Induction Motor (IM) Bearing Fault Detection

Rolling element bearings are commonly used not only in IMs, but also in geneal industrial machinery equipment. Rolling element bearings can be grouped into many categories. For example, based on rolling element types, bearings can be classified as ball bearings, tapered/cylinderal/needle roller bearings. Figure 1.4 illustrates the structure of a ball bearing comprised of an outer ring, an inner ring, rolling elements and a cage to keep the balls uniformly spaced in the bearing. IMs generally consist of bearings with a fixed outer ring and a rotating inner ring that carries motor shaft.
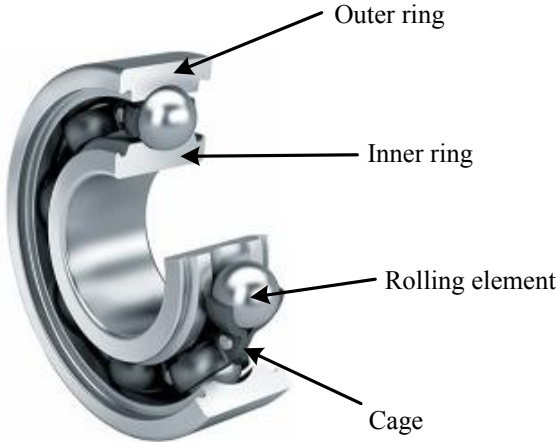
Figure 1.4. Ball bearing structure (reproduced from [23]).

The bearings are subjected to dynamic loading, inherent eccentricities, and material fatigue. Localized bearing defects such as spalling and pitting can occur from the dynamic stresses or external causes such as improper lubrication, contamination, corrosion and improper installation [7]. These localized defects commonly occur in the fixed ring race first, due to its much higher dynamic load/stress cycles than those on other bearing components. The rotating ring race and the rolling elements are also subjected to localized defects, which will degrade IM performance.

IM bearing fault detection can be based on analysis of signals such as vibration, electric current, thermal and acoustic. Among these, vibration and stator current-based analysis has been studied extensively [14, 24]. Unlike other machinery components such as a shaft and a gear, a bearing is a system that consists of inner/outer rings and rolling elements. Its accurate fault diagnosis in bearings still remains a very challenging task in this research field, as its features could be nonlinear and nonstationary especially considering the effects of slide between rolling elements and rings.

Many signal processing techniques in literature are proposed for vibration and current analysis for bearing fault detection, which are summarized below:

(a) Vibration Analysis

If a bearing is damaged, say, a localized defect, as the rolling elements pass through the defect, impacts are generated, which will excite resonance in the support structure [25]. The excitations will generate impact vibrations at frequencies that depend on the shaft rotation speed and the geometry of the bearing. Bearing fault detection techniques aims to extract the fault frequency features related to the localized defect from the vibration signal.

Among these vibration-based techniques, frequency and time-frequency analysis techniques are commonly used. The frequency spectrum is calculated using the Fourier Transform (FT) to investigate the components related to bearing faults [26]. However, spectral analysis assumes stationary signals and fails to catch the transient properties of the signal. Short-time FT

6

is deployed to represent the transient properties of the vibration by calculating the time-frequency map [27]. However, short time FT has limited resolution between time and frequency domains due to fixed time windowing. The wavelet transform (WT) is implemented to study the transient properties of non-stationary signals [28]. For example, in [29], the effectiveness of WT in the detection of different pitting conditions is examined; however, the WT has some leakage effects especially along the ends of the filter banks. Empirical mode decomposition is proposed to represent the signal as a sum of oscillating, zero mean mono-components. For example, Du *et al.* [30] deployed empirical mode decomposition to separate vibration signals caused by surface irregularities and to detect localized defects. However, empirical mode decomposition suffers from mode mixing of closely spaced frequencies. The resonance frequencies of the bearing support structure are enhanced using bandpass filtering [31]. Spectral kurtosis and kurtogram techniques are proposed to determine the support structure resonance frequencies for bearing fault detection [32, 33]. Minimum entropy deconvolution filtering is used to demodulate the noise associated with the signal transmission path [32]. However, the minimum entropy deconvolution filter length strongly influences the effectiveness of the denoising process, whose optimal value depends on transmission path impedance. The envelope analysis method is one of the well-accepted techniques to extract fault frequencies from resonance related frequency bandwidths [34] which has some limitation such as the ineffectiveness in detecting the fault-related modulation under noisy conditions.

Several studies examined the application of Teager-Kaiser energy (TKE) in bearing fault detection using vibration. For example, the TKE-based time domain measures of the vibration signals are examined in [35]. The vibration signal is decomposed into mono-components using empirical mode decomposition and post-processed using TKE for fault feature enhancement [36]. A Teager-Huang transform technique is proposed in [37] to extract fault-related features from vibration signals using a combination of empirical mode decomposition and TKE.

Another challenge in using vibration analysis for IM fault detection is that vibration sensors are usually difficult to be properly installed in an IM with a cylindrical structure. On the other hand, it is difficult to use vibration-based analysis for IM fault detection in rotor bars and electrical systems. The alternative would be the use of current-based analysis.

7

(b) Motor Current Signature Analysis (MCSA)

The accelerometers used for vibration measurements are usually expensive and require direct access to the machinery for installation [44]. Moreover, the mounting location of the vibration sensor also influences the effectiveness of the vibration analysis [45]. Motor current signature analysis (MCSA) is proposed to tackle these problems related to vibration analysis.

MCSA is a non-intrusive diagnostics method that utilizes the stator current signals. IM defects generate fluctuations in the shaft torque; anomalies in the rotor magnetic field could modulate the stator current. These effects can provide fault indicators without direct access to the IM [40]. Many research efforts were taken to apply MCSA for IM fault detection such as broken rotor bars, shorted winding turns, and abnormal air gap eccentricities [4]. Schoen *et al.* [41] used MCSA for bearing fault detection to detect fault frequencies caused by the bearing vibration. In [42], an analytical model was proposed using MCSA for localized IM bearing defect detection. The MCSA were also extensively studied for IM bearing fault detection in [43-48].

Several techniques were also suggested to detect characteristic frequency components for IM fault detection. For example, the Wigner Ville distribution was adopted to track the oscillating instantaneous frequency of the electrical supply to detect the fault-related phase modulations [49] However, Wigner Ville distribution suffers from interference of closely spaced frequency components in multicomponent signals limiting the time and frequency resolution of the analysis. Adaptive noise cancellation using Wiener filtering of the current was implemented to increase the signal-to-noise ratio (SNR) [50]. However, the baseline signal of the healthy motor is required to optimize the filter, and the continuous monitoring of the motor is required to track the statistical properties of the signal. A time-shifting subtraction method was utilized to denoise the periodic components of the signal that are not related to the bearing fault [51]. However, the time-shifted addition method fails to prevent the noisy components in the presence of a nonstationary signal with fluctuating supply harmonics. WT packet was applied to decompose the current signal with low SNR into predetermined frequency bands to investigate the energy levels for fault indicators [52]. However, the selection of WT packet parameters require prior knowledge of the signal properties.

The challenge of MCSA related techniques for bearing defects detection is related to its low SNR. Stator current signals acquired from the IM are dominated by the supply frequency harmonics, rotor slot harmonics, and spectral components related to inherent mechanical tolerances such as imbalances and misalignments. The signals generated from the bearing defects are usually weak compared to the power signals, while the complex signal transmission path from the defect location to the current sensors will lead to even low SNR [53].

1.3 Objectives and Strategies

To tackle the previously mentioned challenges, the goal of this research is to develop an online condition monitoring system for bearing fault detection in IMs using both vibration analysis and MCSA. The focus of the study will be on the analysis of initial bearing fault, which occurs on the outer race of the bearing.

The first objective of this research is to develop a smart sensor system to collect vibration and current signals online. Software solutions will be investigated to develop an MCU-based WSS system with more accurate data sampling, low power consumption, and wireless communication capability.

The second objective is to propose a new signal processing technique, namely generalized Teager-Kaiser energy (GTKE), for bearing fault detection using both vibration and current signal analysis. The GTKE technique aims to detect the characteristic fault frequencies from the vibration and current signals. The proposed GTKE technique will be new in the following aspects: 1) the frequency spectrum of GTKE is investigated for the detection of bearing faults as signal demodulation method, and 2) GTKE is optimized to enhance the bearing fault frequency of the vibration and current signals with low SNR. The effectiveness of the GTKE technique is verified experimentally under different load and speed conditions.

1.4 Thesis Outline

This thesis is organized as follows: Chapter 2 presents the proposed software improvements to tackle the limitations of the existing WSS systems such as the optimal use of battery power, memory extension, reliable wireless communication and consistent data sampling. The developed software will be tested experimentally to verify the performance.

Chapter 3 presents the theoretical basis of the signal models for bearing defect. The fundamentals of the signal modulation, as well as vibration and current based bearing modulation models, are introduced. The existing signal demodulation techniques are also presented.

Chapter 4 discusses the proposed GTKE technique. The effectiveness of the proposed method to enhance the fault related features will be demonstrated by a series of simulation tests. This chapter also includes the overview of the classical TKE technique, provides a mathematical basis on the use of TKE for signal demodulation and summarizes the limitations in processing signals with low SNR.

Chapter 5 presents the experimental results and demonstrates the effectiveness of the examined GTKE technique for bearing fault detection by examining vibration and stator current signals. The robustness of the GTKE technique is tested for IMs under various speed and load conditions. The results are compared with the related techniques.

Chapter 6 summarizes the achievements of this work and conclusions based on the conducted experimental tests. Possible future work to improve the sensor development and the feature extraction method will be provided.

Chapter 2 Smart Sensor Development

In this chapter, a WSS system is developed to meet specific DAQ requirements for IM fault detection, including low power consumption, stable data sampling, sufficient data memory, and reliable wireless communication. Figure 2.1 presents the schematic of the WSS, which consists of a sensor node and a receiver. Figure 2.2 shows the developed MCU-based wireless sensor module with an analog current sensor node and a receiver module with the serial-to-USB communication.
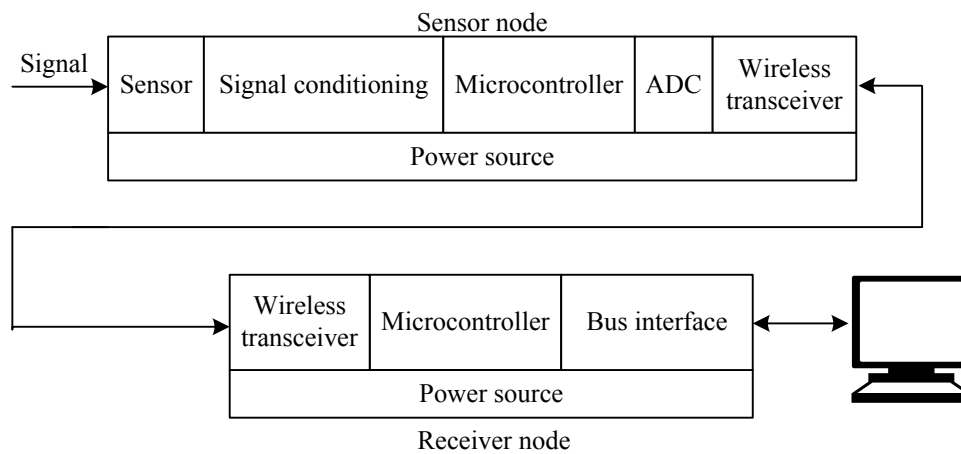
Figure 2.1. WSS with a sensor and a receiver node.
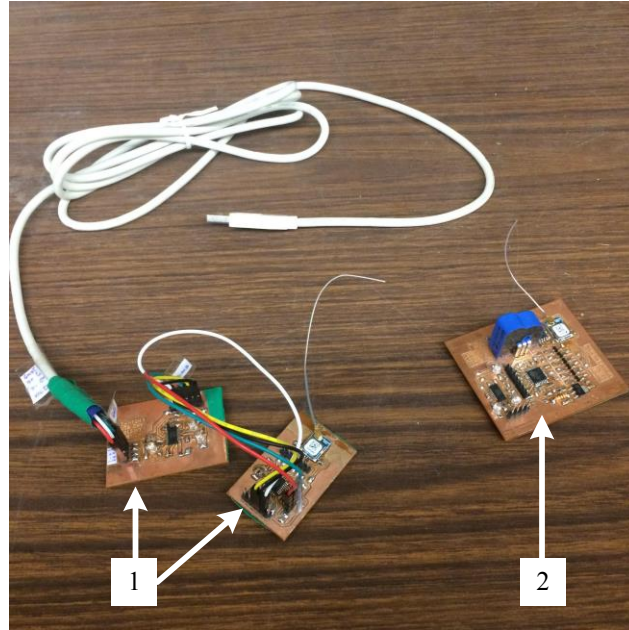
Figure 2.2. The tested WSS system: (1) the receiver module, (2) the sensor module.

2.1 Sensing Element

The tested sensor module is designed for current measurements using analog current sensors. The sensing unit measures the physical current quantity and outputs a voltage output. The sensor voltage output can be digitized using the ADC, as illustrated in Figure 2.3. There are seveal types of analog current sensors available in the market. Among these, Hall effect sensors are commonly used due to their low cost and high performance [15], which will be used in this work. Hall effect is a magnetic phenomenon that can be utilized for current measurement without electrical contact. A Hall effect sensor can be classified as open-loop or closed-loop on the circuit design as shown in Figure 2.4(a,b). Open-loop sensors are cheaper and have simpler circuit designs than their closed-loop counterparts. However, closed-loop sensor provides better frequency response, better immunity to stray magnetic fields and higher range of linearity.
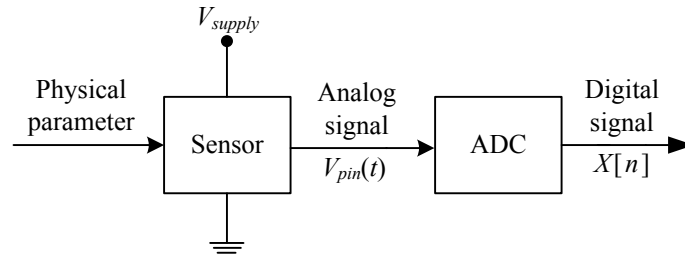
Figure 2.3. Signal measurement using an analog sensor.

The tested sensor module in this work is an LTS 6-NP closed-loop Hall effect current sensor shown in Figure 2.4(a). The current measuring range is ± 6 A. The required voltage supply is 5 V. The sensitivity is 104.16 mV/A.

(a)   (b)
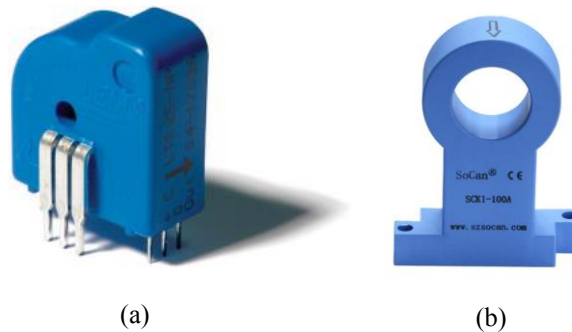
Figure 2.4. Hall effect current sensors: (a) LTS 6-NP closed-loop Hall effect current sensor (reproduced from [54]), (b) SCK1-100A open-loop Hall effect current sensor (reproduced from [55]).

2.2 Microcontroller Unit (MCU)

The function of the MCU is to operate the tasks such as data sampling, data storage, and wireless communication. It can be considered as the brain of the smart sensor system. The MCU in a smart sensor system should meet some requirements, such as ADC capability, stable timing measurement, sufficient computational power, low power consumption, low cost, and availability of development tools for programming [15].

Unlike the general purpose microprocessors in personal computers, an MCU is an embedded processor designed to perform some specific tasks. One of the most commonly used architecture formats for MCUs is Harvard Architecture that utilizes separate, dedicated memories for data and executed program [56]. This architecture provides fast and efficient program execution. Figure 2.5 illustrates the MCU design based on a Harvard Architecture with separate on-chip program read only memory (ROM) and random-access memory (RAM) for data storage operated by the central processing unit (CPU).

The ROM stores the instructions to be executed by the MCU. MCUs with on-chip erasable programmable ROM (EPROM) and flash memories are suitable for testing and debugging procedures of the software development. EPROMs and flash memories can be reprogrammed easily without requiring specialized devices or a formatting process. The RAM is used for data storage. RAMs provide faster data read/write operation than program memory types, regardless of the physical location of the data in the memory, however, data stored in the RAM are lost when the power is turned off [57].
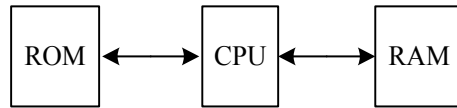
Figure 2.5. MCU design based on Harvard Architecture.

The CPU is the IC that operates the MCU by executing program instructions. These instructions include arithmetic and Boolean logic operations [56]. The data size of the instructions is defined in 2^b-bits depending on the MCU hardware capabilities. MCUs can handle more bits with higher computational power. However, these systems require more complex hardware design, consume higher power, and are more expensive.

Computation operations are based on timing provided by a clock unit. The smart sensor systems require a stable timing for consistent data sampling. Most MCUs include a built-in crystal oscillator-based clock unit. The computation speed of the MCU depends on the clock speed in Hz. High-frequency clocks are faster but require more power to operate.

MCUs communicate with external devices such as sensors and wireless communication modules through digital and/or analog peripherals. In an embedded MCU, the peripherals are hardwired to a specific input/output pin. The MCU communicates digital devices such as ICs and digital sensors through digital peripheral protocols such as an inter-integrated circuit (I2C) or serial peripheral interface (SPI). Analog peripherals include ADC and digital-to-analog converter.

The MCU selected for the WSS in this work is an AVR$^{®}$ family Atmega 328p with low power consumption, relatively high performance, and available development tools. Atmega 328p is an 8-bit MCU with 32 kB reprogrammable flash memory, 1024 byte EPROM and 2 kB static RAM (SRAM). The built-in clock speed is 8 MHz for 3.3 V supply, which can also reach 16 MHz with 5 V supply. Atmega 328p supports both SPI and I2C and has a built-in ADC unit, which can be programmed and operated using a serial to USB interface using an IDE.

2.2.1 Programming Structure

Atmega 328p is programmed using C language. However, C++ based libraries can be included as headers to utilize the object-oriented language structure. The most common approach is to utilize a setup function to initialize variables, which is called when the MCU is connected to the power supply. Then a main function is defined to operate the MCU as long as the MCU is powered on.

2.2.2 Registers

A register is a memory tightly coupled with the CPU's arithmetic and logical unit, which can store data, hold an instruction or specify a pin location [56]. The register values are loaded to the MCU before the program is loaded. Atmega 328p has a 8-bit register architecture, where 16-bit registers are stored in 2×8-bit locations. The registers are utilized to operate ADC, assign input/output pins, and initialize data sampling with the appropriate interrupts.

2.2.3 Interrupts

The normal operation of the MCU executes a sequence of instructions following the main function. However, some high priority events require the disruption of the normal operation. Interrupts are

events that are immediately handled by the MCU [17]. When an interrupt is triggered, the CPU pauses the current task and executes a set of codes called interrupt service routine. The content of the interrupt service routine is specified by the program. It is good practice to keep the interrupt service routine code short to quickly return the MCU to its normal operation.

An interrupt is enabled by an associated register that contains an interrupt enabled bit. The interrupt is triggered when the interrupt flag bit is set, which is unset automatically when the interrupt service routine is executed.

An interrupt can be triggered internally or externally. An internal interrupt is triggered by MCU operations such as the ADC-Conversation-Complete-Interrupt when the ADC of a data point is completed. An external interrupt can be triggered physically by an associated interrupt pin when an electrical signal is applied such as a reset button.

2.2.4 Timers

A timer is a module for timing. A timer module is associated with specific registers. A timer counter is a register with a value that increases/decreases automatically at a predefined rate. The value of the counter changes independently from the MCU without any CPU intervention. The independent timer count makes the time measurement process more accurate.

Timers have different operation modes that can be selected by setting timer control register to a specific value. These values can be found in the MCU data sheet. In normal operation, the counter value is reseted when the maximum bit resolution is achieved. The b-bit timer register is set to zero when the register value reaches the upper limit at 2^b - 1. In the clear-timer-on-compare mode, the upper limit can be set by a program to address an output compare register. Timer registers also include internal interrupts. When the counter reaches the defined maximum value, the CPU triggers a timer interrupt to be handled with an interrupt service routine.

The timers counting rate is adjusted with a prescaler system, which is set by addressing clock-select bits of the timer control register. The prescaler defines the ratio between the clock frequency to the timer cycle frequency, such that;

$$p_{timer} = \frac{f_{clock}}{f_{timer}}$$ (2.1)

where f_{timer} is the frequency at which the timer count is changed, and f_{clock} is the clock frequency that operates the timer unit. The timer can be clocked internally with the MCU clock or externally using an additional clock unit.

The independent counting of the timer and the interrupt feature allow the use of the timer modules for time-sensitive operations such as datasampling. Atmega 328p provides three timer channels with different operation modes and bit resolution. The sampling time for the sensor module will be controlled by the 16-bit Timer-1 count register that can be set to have a count cycle by a prescaler of 8, 64, 256 or 1024.

2.2.5 Digital Peripherals

Digital peripherals are essential for the exchange of data between two devices. There are many protocols for digital communication which can be categorized as parallel or serial communication. Serial communication is the transfer of one bit at a time whereas, in parallel communication, multiple data bits can be simultaneously transmitted through different channels. Serial communication is used commonly for the MCU based applications due to more simple hardware design.

SPI is one of the serial communication protocols supported by Atmega 328p. It is a clocked serial communication protocol that supports data transfer from a master device to multiple slave devices. The communication is deployed one slave at a time. SPI is a synchronous serial communication protocol where the master device provides the clock speed to the slave devices. Figure 2.6 depicts the SPI communication diagram between a master and two slaves. SPI communication is implemented using four serial bus lines:

- CLK (Serial clock): Synchronizes the clock of the master with the slaves for facilitate the data communication.
- MOSI (Master-out-slave-in): Transfers data from the master to the slave.
- MISO (Master-in-slave-out): Transfers data from the slave to the master.

- CS (Chip/Slave select): Selects the slave device to communicate. The CS pin is connected to the voltage supply through a pull-up resistor to prevent pin floating.

The developed WSS in this study utilizes the SPI communication for the wireless antenna and an additional SRAM.
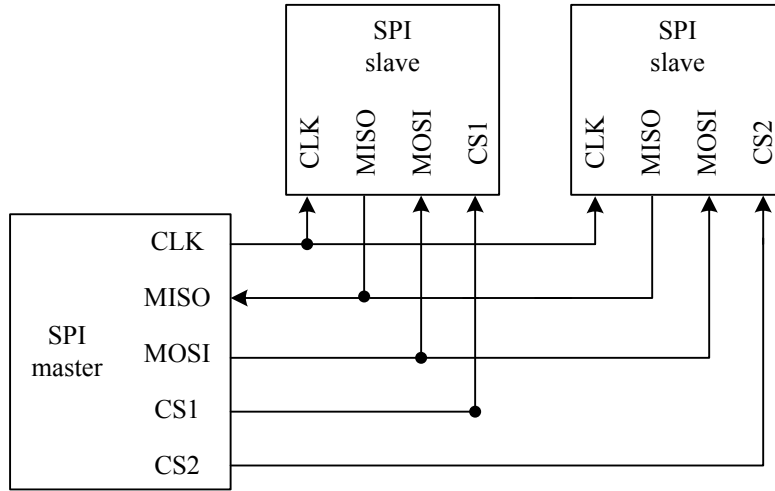
Figure 2.6. SPI communication with one master, two slaves.

2.2.6 Analog-to-Digital Conversion (ADC)

As illustrated in Figure 2.7, ADC is the interface of the MCU to convert an analog signal to a digital counterpart, such that

$$x[n] = \left. \frac{V_{pin}(t)}{Q} \right|_{t=n/f_s} \tag{2.2}$$

where $V_{pin}(t)$ is the pin voltage, n is the data number, f_s is the sampling frequency of the ADC and Q is the analog quantization size, such that

$$Q = \frac{V_{supply}}{2^b} \tag{2.3}$$

where V_{supply} is the voltage of the power supply and b is the bit resolution of the ADC. Increasing bit resolution decreases the quantizing steps that represent a voltage value.

Atmega 328p includes a built-in 10-bit ADC. For a voltage supply of V_{supply} = 5.0 V, the quantization is Q = 4.88 mV. The ADC cannot recognize voltage changes in the analog signal smaller than the quantization size.
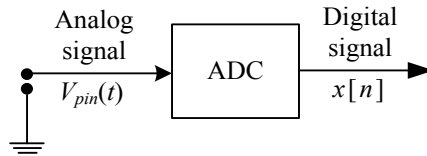
Figure 2.7. ADC based on voltage reading.

ADC in Atmega is programmed using a combination of registers. These registers activate the ADC unit, select an analog pin, start a conversation, and store the ADC reading [58]. Similar to the timer module, the ADC clock is adjusted using a prescaler with division factors of p_{ADC} = 2, 4, 8, 16, 32, 64 or 128. Although decreasing the ADC prescaler increases the speed, the trade-off is a decreased ADC accuracy. The sampling frequency of the ADC is given as

$$f_s = \frac{f_{clock}}{(c_{ADC})(p_{ADC})}$$
(2.4)

where f_{clock} is the MCU clock frequency, c_{ADC} is the number of ADC cycles in one ADC conversation and p_{ADC} is the ADC prescaler. For example, if c_{ADC} = 13 cycles, p_{ADC} = 128 (recommended value), and f_{clock} = 16 MHz, the sampling frequency will be f_s = 9.85 kHz.

The standard programming approach is to operate the data sampling in the normal operation, which is the main script that is run by the MCU. In theory, the data sampling should be consistent. However, in practice, there is no guarantee that the line of code to start the ADC will be executed at the same consecutive time interval. Correspondingly the desired sampling frequency is difficult to achieve.

To overcome this problem, the use of special function register is proposed in this work. As illustrated in Figure 2.8, this register will allow the start of ADC conversation by triggering an interrupt. The trigger source can be linked to the timer module. This allows the timer to control

19

when the ADC conversation is initiated. Using the interrupt triggered by the timer module can ensure that the ADC is called immediately by the MCU without the interference of normal operation.
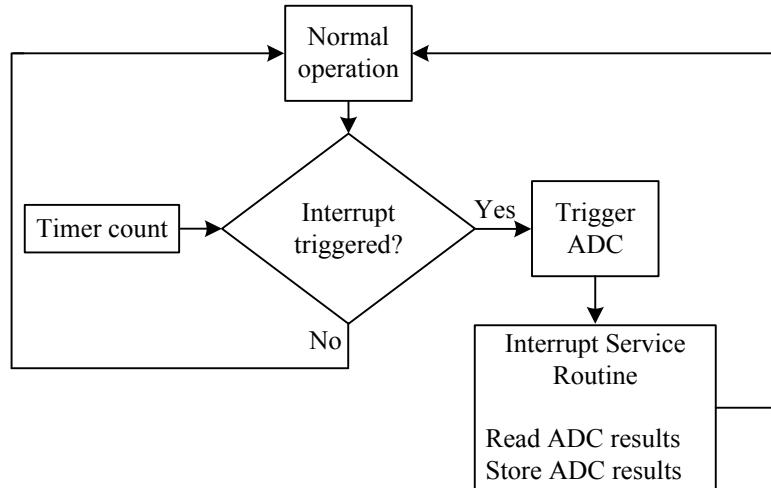
Figure 2.8. Proposed ADC with timer count and data storage.

2.3 Memory Extension

Atmega 328p has a 2 kB internal SRAM for data memory with 8-bit address architecture. The data storage capability is 2048×8-bit data points. In the developed smart sensor system, the data memory is required to store the ADC results. Since the ADC resolution is 10-bits in Atmega328p, for each data point, 2×8-bit memory locations are required to store the high-byte and low-byte values separately, as shown in Figure 2.9. Correspondingly, the 2 kB built-in SRAM of Atmega328p can store a maximum 1024 ADC readings. The data storage capacity decreases further since the variables related to the script are also stored in the data memory. An external SRAM is added using SPI protocol to increase the data storage capacity of the MCU.

10-bit data

1	1	0	1	0	1	0	1	0	1

0	0	0	0	0	0	1	1

8-bit data

0	1	0	1	0	1	0	1
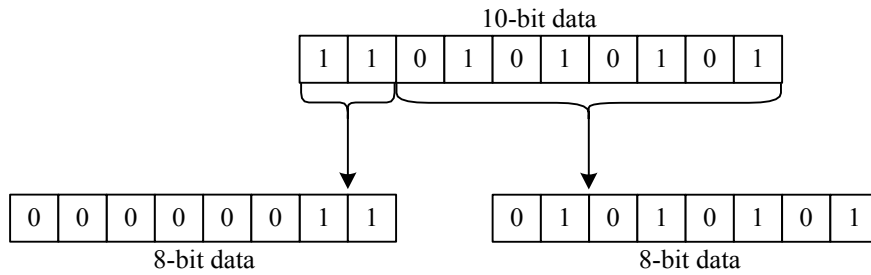
8-bit data

Figure 2.9. Storing of 10-bit data in 8-bit memory locations.

A Microchip 23K256 IC SRAM is selected for this work. The SRAM features include 32,768×8-bit address organization. The corresponding memory of the SRAM for 10-bit ADC is 16,384 data points. If the smart sensor requires further expansion of the data storage capacity, multiple SRAM chips can be used as slave devices (refer to Figure 2.6).

Figure 2.10 shows the breadboard prototype including an Atmega 328-p MCU, 23K256 IC-SRAM, and the Sparkfun FT231X serial-to-USB interface to communicate with the computer. The software related to the SPI communications is verified by testing the breadboard prototype.
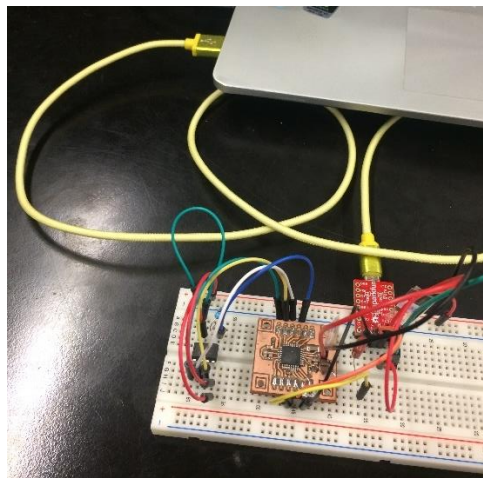
Figure 2.10. SPI communication test setup.

2.4 Sampling Frequency Adjustment

As mentioned in subsection 2.2.6, ADC can be clocked to operate up to 12.5 kHz. However, the addition of external SRAM as the data memory is the bottleneck point of the data sampling. The sampling frequency depends not only on the ADC speed, but also the speed of data storage in the SRAMs through SPI protocol. The overall speed of ADC and the data storage should be considered when determining the minimum time interval to trigger ADC without losing data.

The safe limit for the maximum sampling frequency is approximated by speed testing the ADC in normal operation mode. Figure 2.11 illustrates the proposed algorithm. Atmega 328p offers built-in functions to measure the clock time of the CPU. The maximum sampling frequency can be determined by

$$f_{s,\max} = \left\langle \frac{N}{t_{total}} \right\rangle \tag{2.5}$$

where N is the number of data points, t_{total} is the time duration of the sampling process and $\langle \bullet \rangle$ represents the round-off operator. If $N = 16,384$, and the total time is measured to be $t_{total} = 152.49$ μs, then the corresponding maximum sampling frequency is calculated as $f_{s,max} = 6558$ Hz. This value can be used as a reference for the upper limit of the timer triggered ADC algorithm.
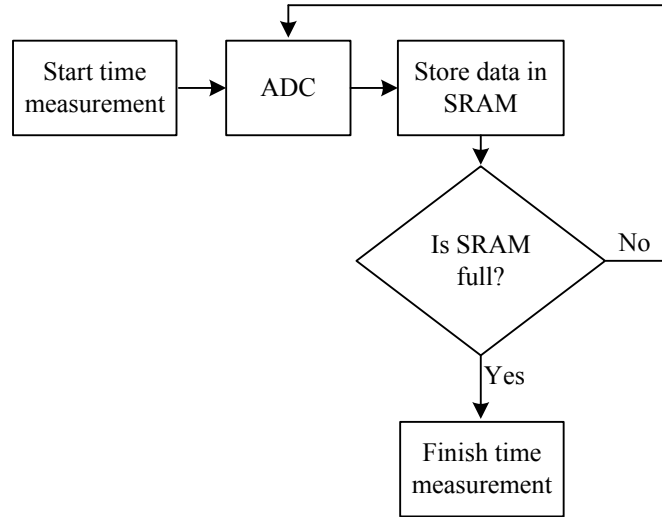
Figure 2.11. The schematic of the algorithm for the SPI speed.

The timer-count to achieve the desired sampling frequency f_s can be calculated as

$$K_{timer} = \left\langle \frac{f_{clock}}{p_{timer} f_s} \right\rangle \qquad (2.6)$$

where f_{clock} is the MCU clock frequency, p_{timer} is the timer prescaler given in Equation (2.1). Based on the approximated $f_{s,max}$, the timer count should be smaller than 2440.

2.5 Wireless Communication

Wireless communication in smart sensor systems allows mobility while reducing installation and maintenance costs. Wireless communication is deployed using RF signals that are categorized by the electromagnetic signal frequency. The frequency bands that the RF ICs operate are labeled by a letter by the IEEE standard [59]. The commonly used RF frequency bands and the corresponding letter labels are presented in Table 2.1.

Table 2.1. RF frequency bands according to IEEE [59].

Letter Designation	UHF	L	S	C	X	K_u	K	K_a
Frequency range (GHz)	0.3 - 1	1 - 2	2 - 4	4 - 8	8 - 12	12 - 18	18 - 27	27 - 40

RF signals are picked up by an antenna. The frequency band selection is made by a radio tuner to tune into the particular frequency band. The information is transmitted using a modulated signal, where the carrier corresponds the frequency band to tune into and the modulating signal contains the transmitted information. In digital wireless communication, the transmitted information is a discrete set of bit values. Increasing the RF frequency range speed up the communication but increase the overall cost and the power consumption [60].

Commonly used WSS communication technologies include Bluetooth, ZigBee and WiFi, which are based on RF signal communication. This work implements a lightweight receiver based handshake protocol that implements RF signal communication. The requirements to implement a wireless communication system in a WSS include low cost, sufficient communication range, and low power consumption. Furthermore, to implement an RF IC to an MCU-based WSS system, the wireless module should be compatible with the MCU digital peripherals such as the SPI protocol.

2.5.1 Microcontroller-based Radio Frequency (RF) Communication

The radio module used in the developed WSS system is A1101R09C integrated RF module by Anaren 1101, which includes the RF IC and the antenna. The IC of the radio module is the CC1101 RF transceiver by Texas Instruments. The frequency selection and the programming are based on IC configurations. The frequency range selected is in UHF band at 900 MHz. The module is operated with 3.3 V supply. A voltage regulator is needed in the design to connect the radio module to the sensor module that operates with 5 V supply voltage.

The CC1101 transceiver is programmable with SPI with four designated SPI pins (refer to Figure 2.6). The IC also includes a built-in output pin to trigger an external interrupt for incoming transmission notification. When the receiver antenna picks up a signal, the interrupt is triggered, and the MCU is programmed to retrieve the data from the RF IC using SPI protocol.

CC1101 data is transmitted and received in packets. Figure 2.12 illustrates the packet structure proposed for the sensor data transmissions. One packet consists of 64 bytes. The first-byte address is used to define the transceiver ID to synchronize the sensor module and the receiver module. The second-byte address defines the packet i to be sent or received. The byte addresses from 3 to 64 store the 10-bit ADC readings. Each 10-bit reading is stored in 2 bytes. Therefore, one packet can contain up to 31 ADC readings. The sensor module can sample up to $N = 16,384$ ADC readings using the external SRAM. The data transmission can be completed using $N / 31 = 529$ packets.
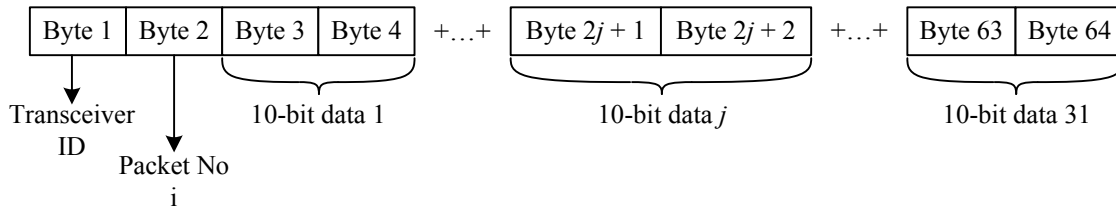
Figure 2.12. Proposed wireless packet structure for CC1101 RF transceiver.

2.5.2 Receive-based Handshake Protocol

When the WSS system is implemented for real-world machinery health condition monitoring, machinery components can interfere with the wireless transmission. These components can block the line of sight of the antenna and cause packet loss in the transmission path. A receiver-based handshake protocol is deployed in this work for the wireless data communication to prevent packet loss. The receiver-based handshake protocol operates on the principle of validating the transmission of each data packet by the receiver.

As illustrated in Figure 2.13, each packet contains a packet number. The receiver requests the data based on this packet number. When the sensor node receives the request, the packet i is

transmitted. In case the request does not arrive at the sensor, or the packet is lost during transmission, the receiver continuously requests the packet i until the packet arrives. When the transmission is complete, the receiver continues with the same procedure for the next packet $i + 1$. This is repeated for every data packet i = 1, 2, ..., 529, to prevent packet loss in wireless transmission.
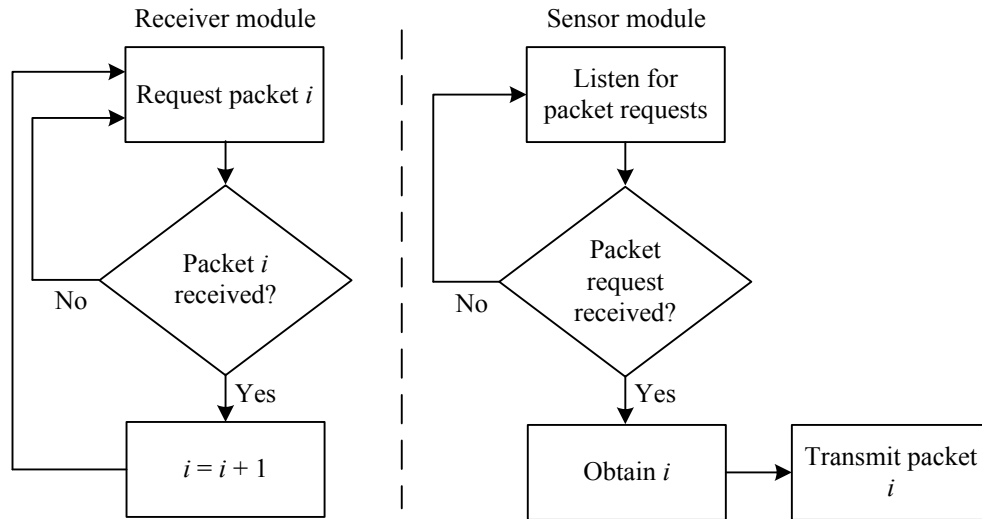
Figure 2.13. Handshake protocol based wireless communication.

2.6 Low Power Consumption

The sensor node of the WSS system is designed to be powered with batteries to collect signals. The power consumption of the system will be another consideration in WSS system design. Power consumption will be reduced by introducing sleep/idle mode to the sensor module when there is no scheduled data collection.

2.6.1 Sleep Mode

Atmega 328p offers a selection of sleep modes with different levels of power consumption. A combination of registers controls these features. Power-down mode offers the minimum power

consumption by putting the MCU to sleep and disabling its functions such as the external oscillator, timer modules, and other I/O pins. Some units require separate handling in code. The ADC, wireless communication unit and the brown-out detector (a safety module required for normal MCU operations) are disabled before entering the sleep mode. Properly using these units can reduce the total current consumption significantly.

2.6.2 Current Consumption

The current consumption for the regular operation mode and the power down mode is measured by connecting an amperemeter into MCU supply line, as illustrated in Figure 2.14. Figure 2.15 shows the current measurement for the normal operation and the power-down mode, respectively. For the Atmega 328p, the respective current consumption in the normal operation and the power-down mode are measured as 16.17 mA and 0.04 mA, which is a significant reduction.
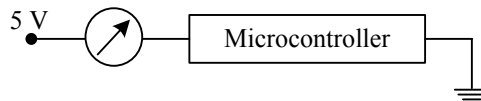
Figure 2.14. Current consumption measurement of the MCU.

(a)   (b)
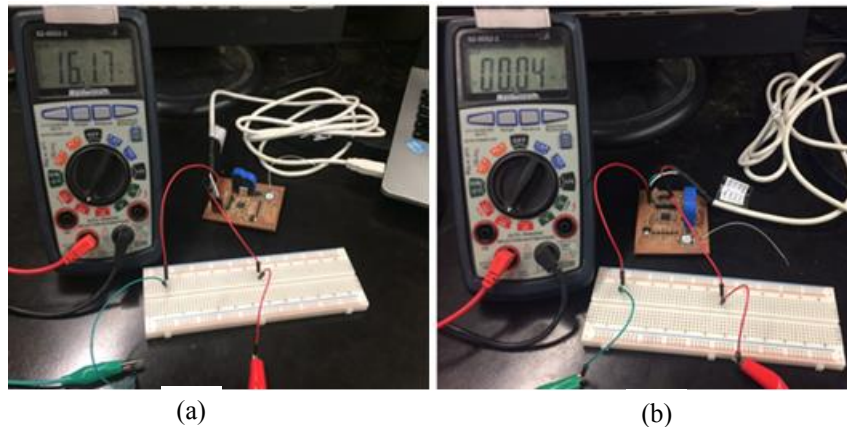
Figure 2.15. Current consumption of the sensor module: (a) normal mode, (b) power down mode.

2.6.3 Exiting the Sleep Mode

When the MCU enters the power-down mode, the normal operation can be resumed by triggering an external interrupt. Although the RF IC includes a built-in external interrupt pin for incoming transmission notifications, the wireless module is powered off in the power-down mode. The MCU is turned on using a particular internal interrupt triggered by the watchdog timer (WDT) that is a timer module with a separate on-chip 128 kHz oscillator designed to limit the maximum time allowed for the power-down mode. The WDT can be enabled as a separate internal interrupt source to track time when the sensor node is turned off and to resume MCU operations. WDT can count up to some specified period, which is selected to count up to 8 seconds in this case. As illustrated in Figure 2.16, the sensor enters in the power-down mode when there is no request for data transmission from the receiver module. The sleep mode is operated using the WDT and the related WDT interrupt.
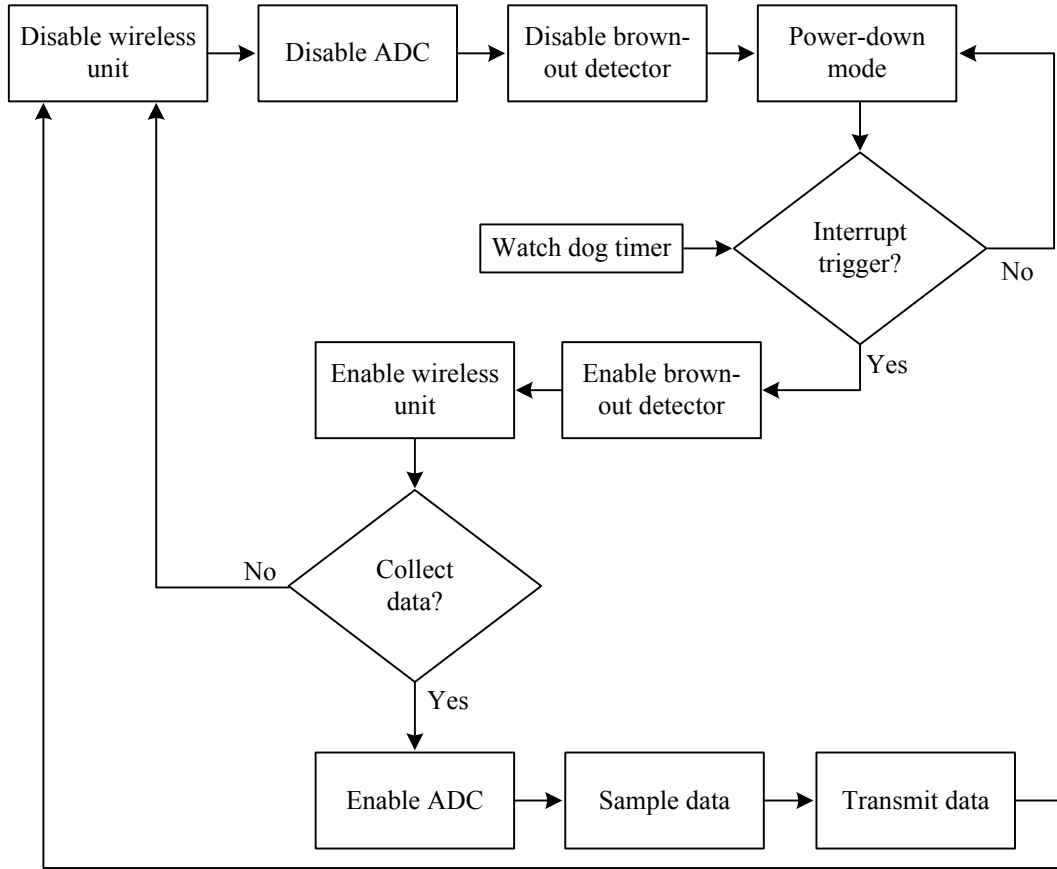
Figure 2.16. Low power mode algorithm.

2.7 Wireless Smart Sensor (WSS) System Verification

The developed WSS system is tested for the wireless communication and stator current sampling using the IM. Figure 2.17 shows the experimental setup used to test the WSS system. The tested IM is a three-phase, 1/3-hp motor (by Marathon Electric). The IM is supplied with 50 Hz supply frequency.

The sensor node is connected to one of the three stator current phases. The 5 V voltage is supplied by a 9 V lithium-ion battery set for longer battery life. A voltage regulator is used to convert 9 V to 5 V for the MCU. 16384 data points are collected in this case and stored in an SRAM, with a sampling frequency f_s = 6550 Hz to test the system, which is maximum sampling frequency of the MCU.

The sensor node is controlled wirelessly using the receiver module that is powered and controlled using the serial-to-USB interface with a computer. The results are displayed using a serial display platform.
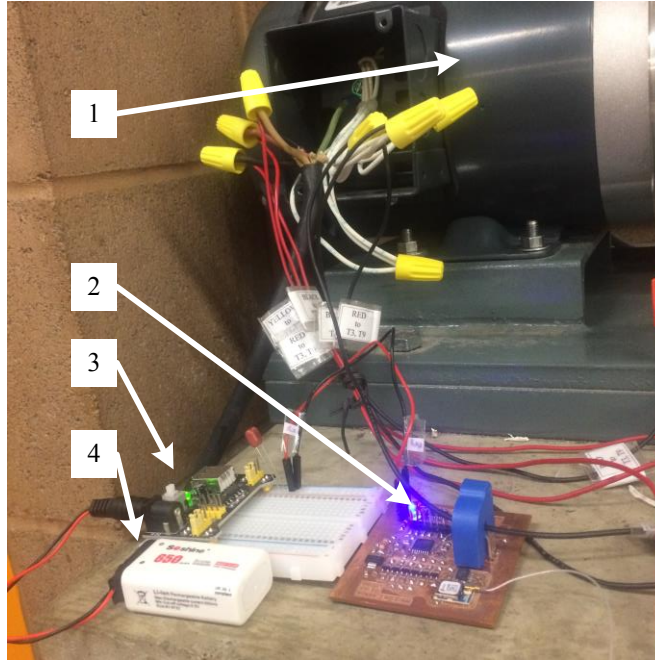
Figure 2.17. Experimental setup: (1) tested IM, (2) wireless sensor module, (3) voltage regulator, (4) power source.

Since IM stator current signal is a sinusoidal wave, any distortions in the signal due to sampling or wireless communication issues will be visible in the time domain. Figure 2.18(a) shows the stator current signal representing a non-distorted sine wave. Therefore, the data sampling and the wireless communication of the WSS system is successful. Figure 2.18(b) shows the frequency spectrum of the collected signal, with the supply frequency at $f_e = 50$ Hz.

The sampling frequency can be caluculated by measuring the total sampling time. Using the MCU's internal oscillator, the time required to collect N data points can be measured in microseconds. For example, if the total measuring time for $N = 16,384$ is $t_{total} = 2501374\mu s$, the calculated sampling frequency is $f_s = N / t_{total} \approx 6549.99$ Hz.
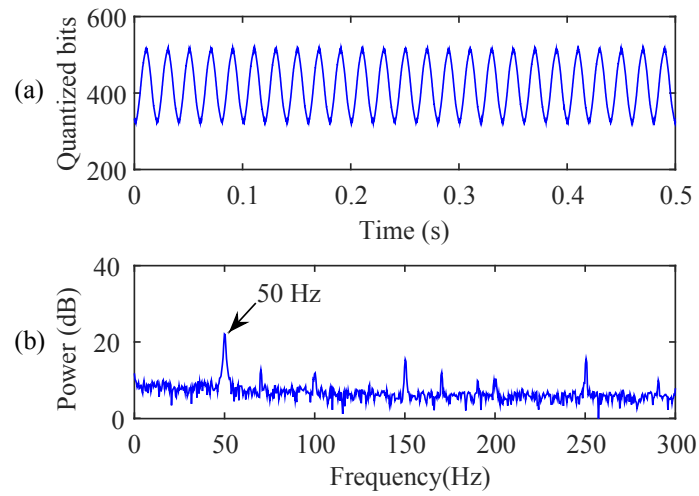
Figure 2.18. WSS system data sampling results: (a) IM stator current signal, (b) the frequency spectrum (the arrow indicates the supply frequency).

2.8 Serial Display Interface

A serial communication-based computer interface is developed in this work to operate the receiver module of the WSS system. The interface consists of a serial display to communicate with any MCU that is capable of serial communication. Figure 2.19 shows the screenshot of the interface in operation.
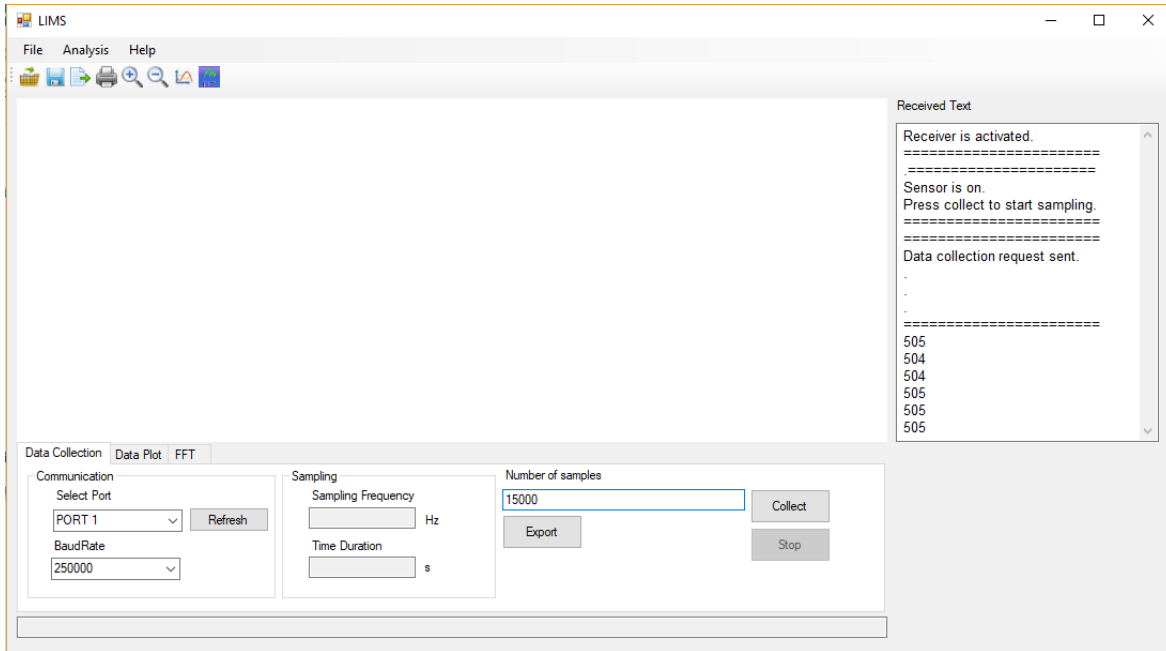
Figure 2.19. A serial communication based interface.

Chapter 3 Induction Motor (IM) Bearing Fault Models

The IM faults can result in modulation of the vibration and stator current signals [61, 62]. Bearing fault detection relies on the detection and examination of the charateristic features related to the IM defect. In this chapter, the fundamentals of signal analysis and system models are reviewed. This study focuses on fault detection in rolling element bearings, using both the vibration and current signals.

3.1 Analysis of the Signal Modulation

Modulation is defined as the time variation of some specific properties of a signal. A modulated signal consists of a carrier and a modulating envelope. Modulation is categorized into two groups:

- Amplitude modulation (AM): A carrier signal with varying envelope.

- Angle modulation: A carrier signal with a varying angle. Angle modulation is further categorized into frequency modulation and phase modulation.

When the vibration or current signals are investigated for an IM with a mechanical fault, the dominant modulation mechanism is AM of the carrier signal envelope.

3.1.1 Amplitude Modulation (AM)

An AM signal is defined as a signal with an envelope varying with time, such that

$$x_{AM}(t) = A_m(t)\cos(2\pi f_c t + \theta) \tag{3.1}$$

where $A_m(t)$ is the envelope function, and f_c is the carrier frequency, and θ the phase of the carrier signal that is assumed to be equal to zero for simplicity. The envelope can be modeled as a sinusoidal wave plus a DC offset to ensure $A_m(t)$ is always positive, such that

$$A_m(t) = 1 + \kappa\cos(2\pi f_m t) \tag{3.2}$$

where f_m is the modulation frequency, and $\kappa \in [0, 1]$ is the modulation index. Increasing κ increases the strength of the modulation signal. Substituting Equation (3.2) into Equation (3.1) gives

$$x_{AM}(t) = \cos(2\pi f_c t) + \kappa \cos(2\pi f_m t)\cos(2\pi f_c t) \tag{3.3}$$

which can be further expanded as

$$x_{AM}(t) = \cos(2\pi f_c t) + \frac{\kappa}{2}\left(\cos\left(2\pi(f_c - f_m)t\right) + \cos\left(2\pi(f_c + f_m)t\right)\right) \tag{3.4}$$

Thus, AM signal is represented as the summation of sinasoidal functions with frequencies f_c, and the modulation sidebands ($f_c \pm f_m$). Figure 3.1 depicts an AM signal with time-varying envelope and the corresponding frequency spectrum with modulation sidebands. It can be noted that the spectral components corresponding to the modulating frequency f_m will not be recognized directly on the spectrial map, but becomes sidebands around the carrier frequency f_c. The modulation frequency can be obtained using signal demodulation techniques.
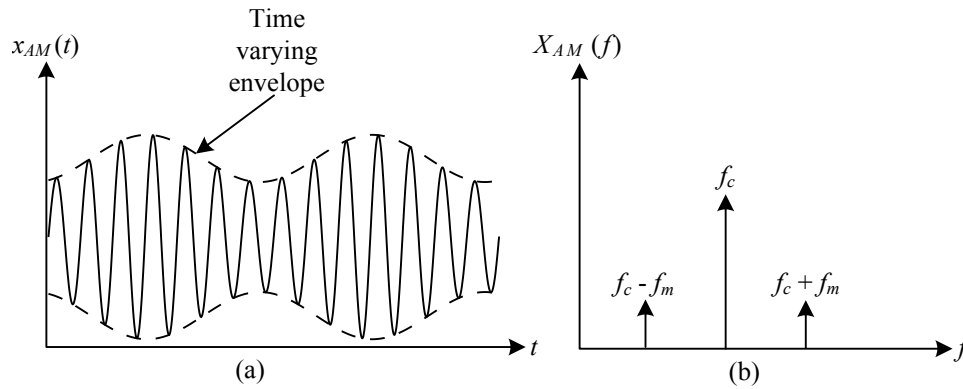
Figure 3.1. Example of an AM signal: (a) Time domain, (b) Frequency domain

3.1.2 Envelope Detector-based Demodulation

The envelope detector is proposed initially as a circuit scheme to demodulate analog signals for AM radios [63]. Firstly, any DC offset is removed to obtain the zero mean AM signal. The absolute value of the signal is obtained by a rectifier consisting of a diode and a capacitor. The signal is

then low pass filtered using a resistor-capacitor circuit. The output is the signal envelope that contains the modulating frequency. Digital signals can be demodulated using the same procedure with digital filters. Figure 3.2 illustrates the demodulation of a zero mean digital AM signal using an envelope detector. The signal is rectified by calculating the absolute value, and the envelope is obtained by using a digital low pass filter.
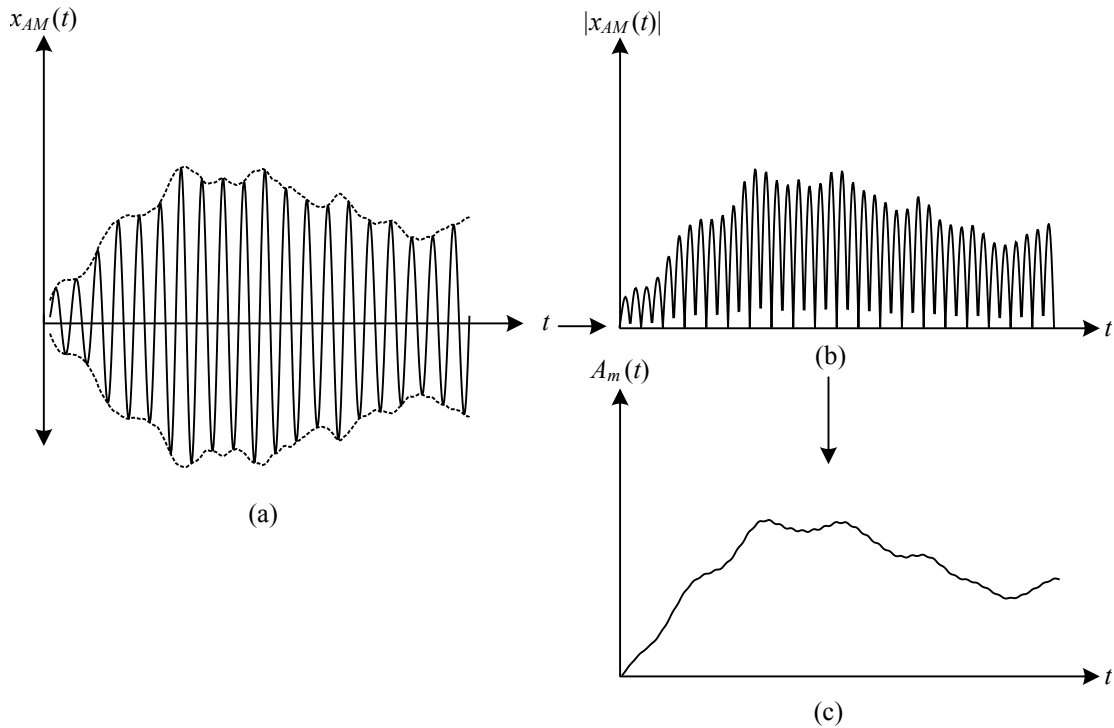
Figure 3.2. Demodulation using an envelope detector: (a) AM signal, (b) signal passed through a rectifier, (c) extracted envelope by the lowpass filter.

3.1.3 Hilbert Transform and Signal Demodulation

The envelope analysis accuracy can be improved using advanced signal processing methods. One such technique is based on the expansion of the original signal into an analytical signal, such that

$$x_a(t) = x(t) + jH\big(x(t)\big) \tag{3.5}$$

35

where x_a is the analytical signal, $x(t)$ is the original signal, $j = \sqrt{-1}$ and $H(\bullet)$ represents the Hilbert transform, which can be calculated as

$$H(x(t)) = \frac{1}{\pi} \int_{-\infty}^{+\infty} \frac{x(\tau)}{t-\tau} d\tau \tag{3.6}$$

where τ is the integration variable for time t.

For the AM signal given in Equation (3.1), then the Hilbert transform can be calculated as [14]

$$H(x_{AM}(t)) = A_m(t)\sin(2\pi f_c t) \tag{3.7}$$

Moreover, the corresponding analytical signal is given as

$$x_{AM_a} = A_m(t)\big(\cos(2\pi f_c t) + j\sin(2\pi f_c t)\big) \tag{3.8}$$

By some manipulation, $A_m(t)$ can be obtained by calculating the absolute value of the analytical signal, such that

$$\left| x_{AM_a} \right| = \sqrt{A_m^2(t)\big(\cos^2(2\pi f_c t) + \sin^2(2\pi f_c t)\big)} = A_m(t) \tag{3.9}$$

3.2 Vibration-based Bearing Models

Even if a rolling element bearing is healthy, it generates vibration in operation as contact dynamics between rolling elements and rings vary with time. Thesurface of the raceways and the bearing rings also have imperfections caused by the manufacturing tolerances. The level of vibration is influenced by the rotation speed of the shaft and the carried load. In bearing fault detection, those vibration components not generated by a defect would be considered noise. Unlike a shaft or a gear which are components, the rolling element bearing is a system consisting of multiple moving parts. Furthermore, the position of the rolling elements carrying the load change with the rotation of the shaft, giving rise to vibration signals that are nonlinear and nonstationary. However, when

a localized defect occurs in the bearing, the vibration levels increase due to impact resonances; effective fault detection techniques should be developed by examining the vibration signatures of the bearing defect.

3.2.1 Vibration Signature of a Bearing Defect

A localized defect frist occurs on the fixed race or outer ring race in general. As the rolling elements pass through the damaged location, the resulting impacts excite the resonance in the support structure. The defect leads to the generation of short duration impulses in the vibration with unique characteristics that depend on the location of the defect, the speed of rotation and the geometry of the bearing.
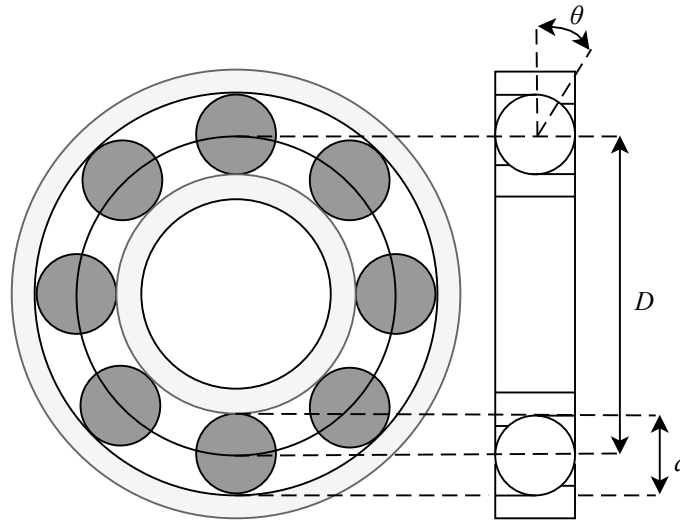
Figure 3.3. The geometry of a ball bearing (D = pitch diameter, d = ball diameter, θ = contact angle).

Spectral analysis of the vibration signal is one of the most commonly used techniques for bearing fault detection. It is based on the extraction of fault characteristic frequencies. Consider a rolling element bearing as shown in Figure 3.3, the characteristic frequency of a defect on the fixed outer race will be

$$f_{od} = Z \frac{f_r}{2}\left(1 - \frac{d}{D}\cos(\theta)\right) \tag{3.10}$$

where d is the ball diameter, D is the pitch diameter, θ is the contact angle, Z is the number of balls, and f_r is shaft rotating speed in Hz.

These bearing dimensions are provided by the bearing manufacturers and can be obtained based on the bearing model number. However, the IM bearings are concealed within the motor casing, and in some cases, the bearing model may not be available to the diagnostician. Correspondingly, the outer race defect frequency can be approximated for most bearings, such that [64]

$$f_{od} \approx 0.4 Z f_r \tag{3.11}$$

3.2.2 Envelope Analysis

Fault related features are contained in collected vibration signal, which is the repetition of the impulses, not the resonance frequencies of the bearing support structure. However, the frequency spectrum obtained directly from the raw vibration signal is usually dominated by the former. The spectral contents of the raw vibration signal are further modulated by the residual imbalances in the shaft and the gears signals.

One method to extract the repetition frequency is to extract the envelope of the impulses. In this approach, the bearing vibration signature is modeled as an AM signal. Figure 3.4 shows the typical vibration signal consisting of a series of impulses generated by the outer race bearing defect and the corresponding signal envelope that represents the impulse repetition.

Outer race defect signal

$1/f_{od}$
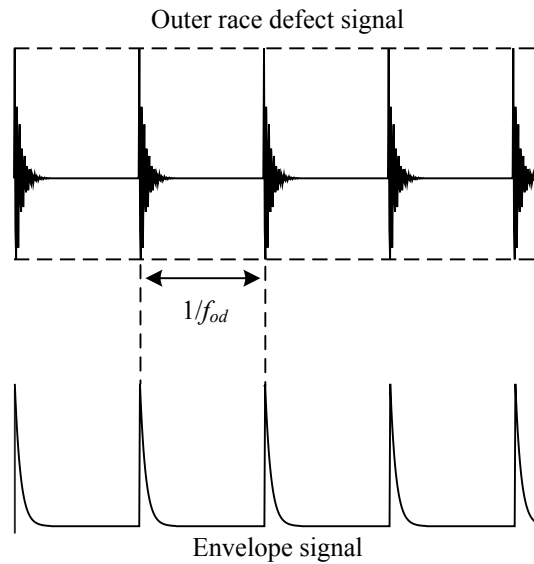
Envelope signal

Figure 3.4. Simulated vibration signal of an outer race bearing defect and the corresponding signal envelope.

The envelope analysis technique is a benchmark method for vibration based bearing fault detection. The premise of the envelope analysis is the extraction of the fault-related information by demodulating the resonance excitations using the related techniques, as stated in subsection 3.1.2 and subsection 3.1.3. The fault-related features are further enhanced by bandpass filtering the frequency resonance frequencies. Bandpass filtering allows keeping the signals at resonance frequencies but prevents the masking of the fault characteristic frequencies by other high-level signals not related to the defect. The effectiveness of the envelope analysis depends on the selection of the proper frequency band.

3.3 Current-based Bearing Models

In a healthy IM, the stator current is a sinusoidal wave dominated by the supply frequency and its harmonics. When a mechanical fault occurs in the IM, the stator current is modulated by the several factors such as the variation of the torque load and the fluctuations in the air-gap eccentricities. Similar to the vibration signal, each mechanical fault generates a particular feature that contains

fault-related information. The challenge of mechanical fault detection using MCSA is the detection of weak fault-related features masked by high-level signals.

3.3.1 Stator Current Signature of a Bearing Defect

The IM works on the principle of electromagnetic induction. The alternating current supplied to the IM creates a rotating magnetic field. The changing magnetic field induces a current flow in the rotor bar consisting of electrically conducting material. The result is a magnetomotive force that rotates the rotor and the shaft with speed slower than the synchronous speed of the magnetic field. The magnetomotive force depends on the air-gap length between the stator and the rotor of the IM. When an air-gap eccentricity occurs due to the radial displacement of the rotor as illustrated in Figure 3.5, the air-gap length between the stator and the rotor varies with the rotation of the shaft.
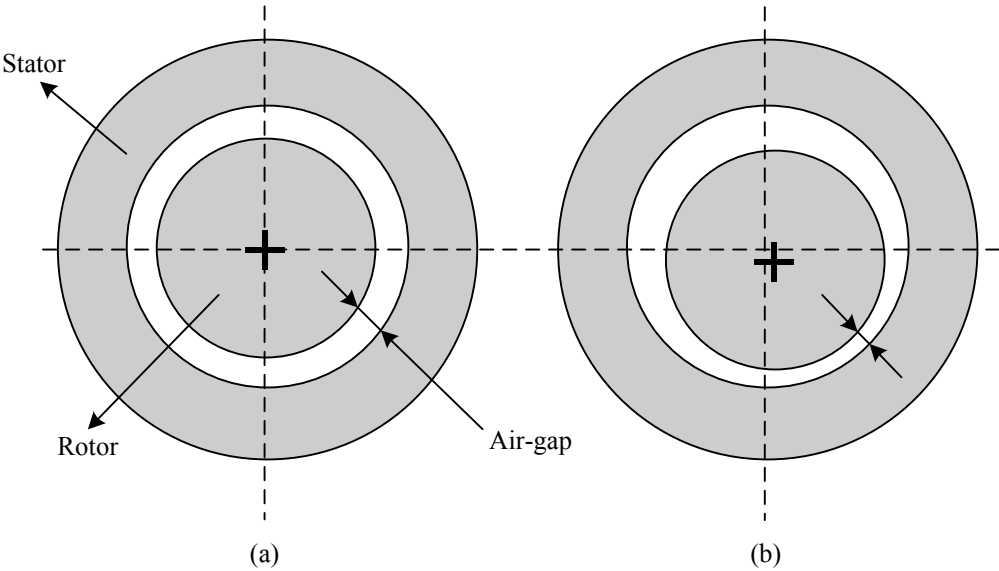
Figure 3.5. Air-gap eccentricity due to the rotor displacement: (a) Normal motor, (b) Motor with air-gap eccentricity

The variations in the air-gap length affect the air-gap flux density. This causes a variation in the inductance of the IM and produces additional spectral harmonics in the frequency spectrum of the stator current, such that

$$f_{ecc} = |f_e \pm k f_r|$$

where $k = 1,2,3,\ldots$; f_e is the supply frequency, and f_r is the shaft speed.

In an IM, the rotor is attached to the shaft. Any displacement in the shaft results in the displacement of the rotor. In a bearing with an outer race defect, when there is no contact between the rolling elements and the defect, the rotor is centered as illustrated in Figure 3.6.(a). As the rolling elements pass through the defect, the rotor center is displaced, as shown in Figure 3.6.(b). The displacement causes an air-gap length, which in turn introduces frequency components in the stator current, such that

$$f_{ecc;or} = |f_e \pm k f_{od}|$$

(3.13)

where f_{od} is the fault characteristic frequency, defined in Equation (3.10).
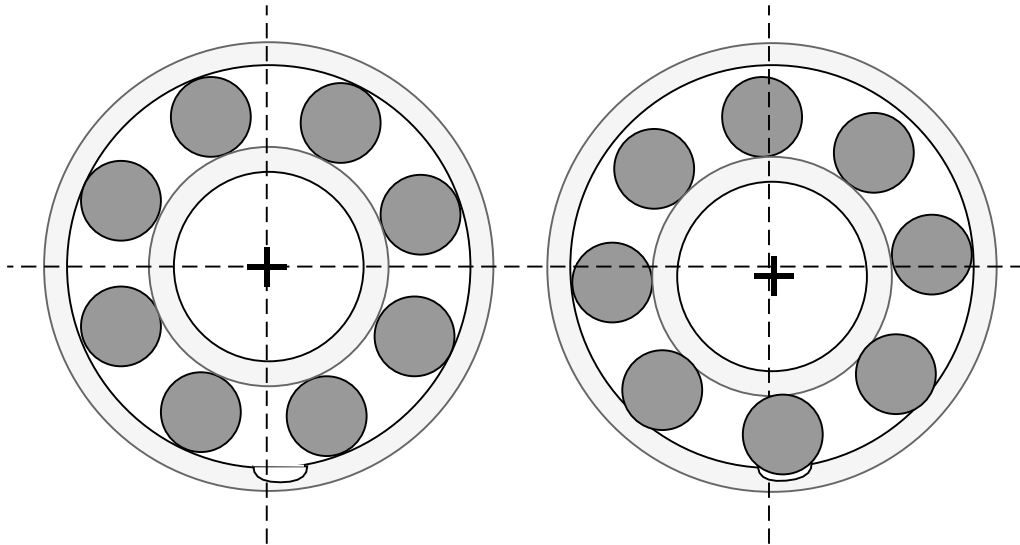
Figure 3.6. Rotor displacement caused by the bearing defect (the fault size is exaggerated for better illustration).

A common method for bearing fault detection is based on the analysis of the sidebands given in Equation (3.13). The challenge is the detection of modulation sidebands related to the fault if the SNR is low.

3.3.2 Demodulation

Based on Equation (3.13), the stator current of the IM with outer race bearing defect can be calculated as

$$I(t) = \cos\left(2\pi f_e t\right) + \sum_{k=1}^{\infty} \cos\left(2\pi(f_e + k f_{od})t\right) + \cos\left(2\pi(f_e - k f_{od})t\right) \tag{3.14}$$

In signal processing, the stator current of an IM with a bearing defect is an AM signal with carrier frequency at the supply frequency f_e and the modulation frequency f_m at the vibration characteristic frequency. The vibration-based fault characteristic frequency can be extracted using appropriate demodulation techniques [42]. However, it should be noted that the carrier frequency in this case can be lower than modulating frequency, unlike the vibration signal where the resonance frequencies are usually higher than the fault frequency.

Although the use of stator current for bearing fault detection has been investigated by many researchers [40, 52], the effectiveness of the demodulation techniques for bearing fault detection has not been fully studied. In [65], the authors investigated the effectiveness of the vibration envelope analysis used previously by bandpass filtering the frequency bands with high kurtosis. However, it did not provide any explanation of the relationship between the kurtosis value and fault information. Dalvand *et al.* [51] examined the envelope spectrum of the denoised stator current signal to demodulate spectral components corresponding to the vibration-based fault characteristic frequency. However, their results based on envelope spectrum provide no clear improvement over the frequency spectrum of the raw signal.

To tackle the related problems, a new demodulation technique will be proposed in the next chapter to extract the weak vibration signal modulating the supply frequency, and enhance the fault-related information.

Chapter 4 Proposed Generalized Teager-Kaiser Energy (GTKE) Technique

A new GTKE technique is proposed in this chapter to detect the modulating frequency components in signals with low SNR for IM fault detection. Its processing procedures are illustrated in Figure 4.1. Different from the classical TKE method that demodulates the signal using the TKE operator, the proposed GTKE technique implements the GTKE operator that can be optimized to detect a modulation frequency under noisy condition.
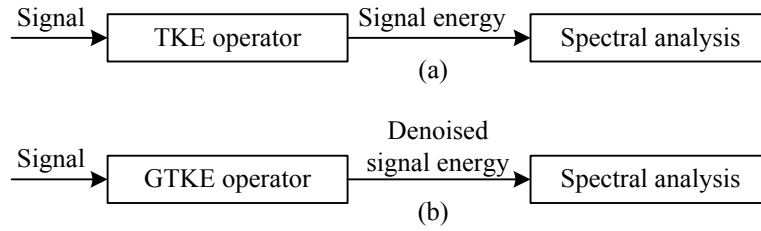
Figure 4.1. Envelope detection: (a) TKE technique, (b) Proposed GTKE technique.

4.1 Analysis of Classical Teager-Kaiser Energy (TKE) Technique

In general, signal energy is calculated in the form of $E = |x(t)|^2$, where the energy required to generate the oscillating signal is proportional to the square of the amplitude only. However, this expression is incomplete since the energy required to generate a signal increases at higher frequencies. Consider the free vibration of a spring-mass system. The equation of motion is given as

$$\ddot{x} + \frac{k}{m}x = 0 \tag{4.1}$$

where $\dot{x}$ and $\ddot{x}$ represent the respective first and second time derivative, k is the spring constant, and m is the mass. The simple harmonic motion of the system is given as

$$x(t) = A\cos(\omega t) \tag{4.2}$$

where A is the amplitude and ω is the angular frequency in rad/s such that $\omega = \sqrt{\dfrac{k}{m}} = 2\pi f$. The total energy of the system can be calculated by

$$E = \frac{1}{2}kx^2 + \frac{1}{2}m\dot{x}^2 \tag{4.3}$$

Substituting Equation (4.2) into Equation (4.3) gives

$$E = \frac{1}{2}mA^2\omega^2 \tag{4.4}$$

Thus, the energy of oscillation is proportional not only to the square of the amplitude but also to the square of the frequency.

4.1.1 The TKE Operator

The TKE operator was first introduced in by Kaiser in [66] as an on-the-fly energy calculation method for signals. It is a nonlinear differential operator to tracks the instantaneous energy of the signal. For a continuous signal $x(t)$, the TKE is defined as

$$\Psi\big(x(t)\big) = \dot{x}^2(t) - x(t)\ddot{x}(t) \tag{4.5}$$

which can be expanded further as

$$\begin{aligned}
\Psi\big(x(t)\big) &= (-A\omega\sin(\omega t))^2 - A\cos(\omega t)(-\omega^2 A\cos(\omega t)) \\
&= A^2\omega^2\big(\sin^2(\omega t) + \cos^2(\omega t)\big) \\
&= A^2\omega^2
\end{aligned} \tag{4.6}$$

Thus, energy estimation based on TKE operator includes the amplitude and the frequency. For a discrete signal $x[n]$, the TKE can be calculated by

$$\Psi\big[x[n]\big] = x^2[n] - x[n+1]x[n-1] \tag{4.7}$$

The TKE operator is based on the estimation of the instantaneous signal energy using the discrete difference operation in Equation (4.7), which can be used to examine the spectral components.

4.1.2 The TKE and Demodulation

The TKE operator can track the energy required to generate a modulated signal [67-69]. The TKE based demodulation techniques in literature rely on the computation of instantaneous frequency and the instantaneous amplitude to separate the carrier signal from the modulating signal. However, the TKE itself contains information related to the modulation and can be used to detect the signal envelope. Consider the AM signal defined in Equation (3.4). The respetive first and second time derivatives of the signal can be calculated as

$$\dot{x}_{AM}(t) = -A\left(\frac{\kappa}{2}\left((\omega_c + \omega_m)\sin\left((\omega_c + \omega_m)t\right) + (\omega_c - \omega_m)\sin\left((\omega_c - \omega_m)t\right)\right)\right) \\ -Aw_c \sin(\omega_c t) \tag{4.8}$$

$$\ddot{x}_{AM}(t) = -A\left(\frac{\kappa}{2}\left((\omega_c + \omega_m)^2 \cos\left((\omega_c + \omega_m)t\right) + (\omega_c - \omega_m)^2 \cos\left((\omega_c - \omega_m)t\right)\right)\right) \\ -A\omega_c^2 \cos(\omega_c t) \tag{4.9}$$

By substituting Equations (4.8) and (4.9) into Equation (4.5), the TKE of the signal will be

$$\Psi(x_{AM}) = A_1\left(\cos\left((2\omega_c + \omega_m)t\right) + \cos\left((2\omega_c - \omega_m)t\right)\right) \\ + A_2\left(\omega_c^2 \cos(2\omega_m t) + \omega_m^2 \cos(2\omega_c t)\right) + A_3 \cos(\omega_m t) + A_4 \tag{4.10}$$

where

$$A_1 = \frac{A^2 \kappa}{4} \omega_m{}^2$$

$$A_2 = \frac{A^2 \kappa^2}{2}$$

$$A_3 = \frac{A^2 \kappa}{2} (4\omega_c{}^2 + \omega_m{}^2)$$

$$A_4 = \frac{A}{2} (3\omega_c{}^2 + \omega_m{}^2)$$

(4.11)

Based on Equation (4.10), the frequency domain representation of the TKE will consist of several spectral components, including the sidebands at $(2f_c \pm f_m)$, the second harmonic of the carrier frequency $2f_c$, the modulating frequency at f_m, and its second harmonic at $2f_m$. The presence of the modulating frequency in the frequency spectrum indicates that the TKE operator can detect the envelope of the signal.

To test the effectiveness of the TKE technique as an envelope detector, an AM signal is simulated based on Equation (3.4), whose properties are summarized in Table 4.1. Figure 4.2 shows the simulated AM signal and the corresponding TKE, respectively. The similarity between the signal envelope and its TKE can be observed. Figure 4.3 illustrates the frequency spectrum of the AM signal and the corresponding frequency spectrum of the TKE. As predicted in Equation (3.4), the modulation sidebands near the carrier frequency can be observed, while the modulating frequency is not present in the spectrum. On the contrary, the frequency domain of the TKE contains fundamental frequency and its second harmonic of the modulating signal, as predicted in Equation (4.10).

Table 4.1. Simulated AM signal information.

f_m	f_c	κ	A	f_s	N
10 Hz	50 Hz	0.3	1	6000 Hz	5000
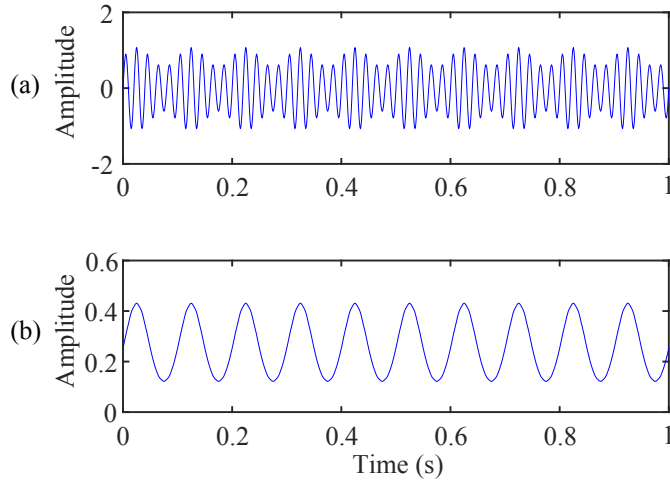
Figure 4.2. (a) The simulated AM signal, (b) the TKE of the simulated AM signal
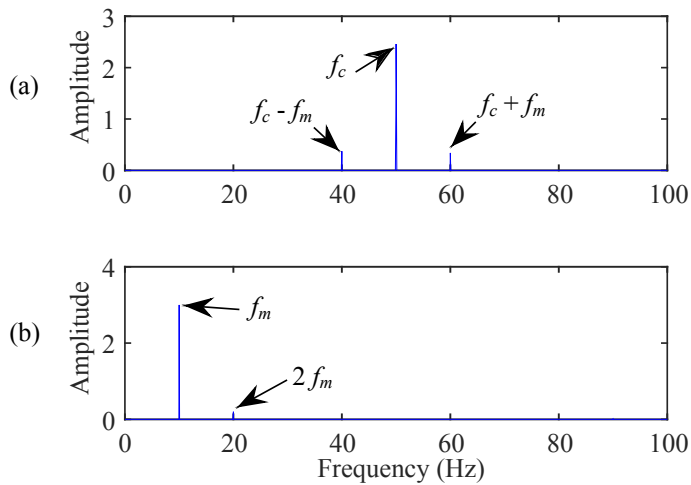
Figure 4.3. The frequency spectra: (a) the simulated AM signal, (b) the corresponding frequency spectra.

4.1.3 Noise Sensitivity

Consider a discrete signal $x[n]$ with additive zero-mean Gaussian noise $N[n]$, with variance σ_N^2, such that

$$\hat{x}[n] = x[n] + N[n] \tag{4.12}$$

The expectation of the discrete TKE will be [66]

$$E\left[\Psi\left[\hat{x}[n]\right]\right] = \Psi\left[x[n]\right] + \sigma_N^{\,2} \tag{4.13}$$

The TKE of the signal with added noise deviates from the clean signal $x[n]$ by the variance of the noise. The sensitivity of the TKE operator to noise can also be estimated from examining Equation (4.6), where the instantaneous energy is proportional to the signal frequency. This implies that the TKE operator is sensitive to high-frequency noise such as spikes and sudden changes. Although the noise sensitivity problem cannot be fully solved, the TKE operator can be modified to decrease the noise sensitivity over some frequency bandwidth, which can enhance particular spectral components in the signal by reducing the sensitivity to high-frequency noise.

4.2 Generalized Teager-Kaiser Energy (GTKE) Technique and Optimization

The signals collected from the IM have low SNR for IM fault detection [70]. An effective fault detection technique should be able to compensate for the noise masking fault information. The proposed GTKE technique in this work aims to increase the robustness of classical TKE operator against noise [71].

4.2.1 The Proposed Generalized Teager-Kaiser Energy (GTKE) Technique

GTKE is defined by introducing a resolution parameter, such that

$$\Psi_k\left[x[\mathrm{n}]\right] = x^2[n] - x[n-k]x[n+k] \tag{4.14}$$

where k is an arbitrary integer referred to as the lag that is used to adjust the distance between the samples. When $k = 1$, the extension reduces to the classical TKE operator.

4.2.2 Optimal Lag Parameter Estimation

The lag k of the GTKE technique can be adjusted to enhance a targeted frequency bandwidth. The optimization of the lag k for a particular modulating frequency can be conducted by analysing a series of simulated signals. An AM signal with additive Gaussian noise is simulated in the form

$$x_{AM}[n] = A\cos[2\pi f_c n](1 + \kappa\cos[2\pi f_m n]) + N[n] \tag{4.15}$$

where $N[n]$ is the additive noise.

Two conditions are considered for the simulations:

1) The AM signal with $f_m < f_c$. This is the general case for modulated signal, which can represent the bearing fault model for the vibration signal.

2) The AM signal with $f_m > f_c$. This condition could be specific for the IM stator current signal with bearing defect where the bearing defect corresponds to a higher frequency than the carrier signal with the electrical supply frequency.

For condition 1), the properties of the simulated signal are summarized in Table 4.2. These values are selected to simulate an AM signal with low SNR and weak modulating signal. Figure 4.4 shows the time domain and the corresponding spectral representations of the simulated signal. The modulating frequency of the signal is smaller than the carrier frequency. Correspondingly, the modulation sidebands are generated above and below the carrier frequency 800 Hz in this case. The right-hand sideband is masked by the noise, while the left-hand sideband can be barely detected.

49

Table 4.2. AM signal simulation parameters for $f_m < f_c$.

f_m	f_c	κ	A	f_s	N	σ_{noise}
150 Hz	800 Hz	0.03	1	6247 Hz	16000	0.3
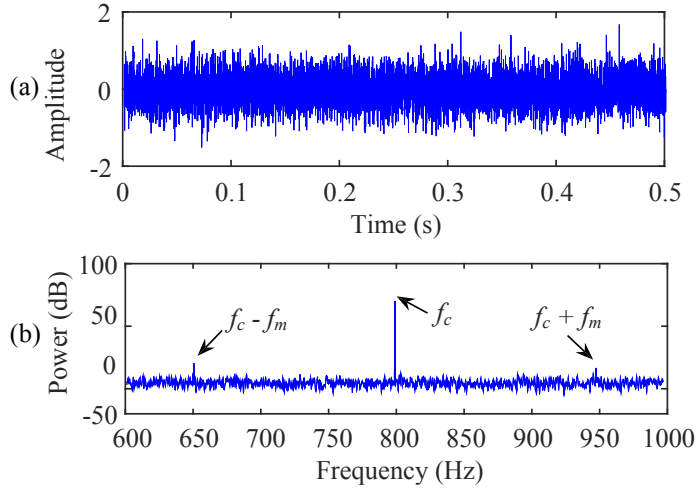
Figure 4.4. (a) The simulated AM signal with additive Gaussian noise, (b) the corresponding frequency spectrum.

The processing results using the TKE operator is presented in Figure 4.5. From Equation (4.10), the predicted modulating frequency should be present in the frequency domain representation of the TKE. However, the modulation signal is masked by the noise and TKE operator failed to detect the modulating frequency.
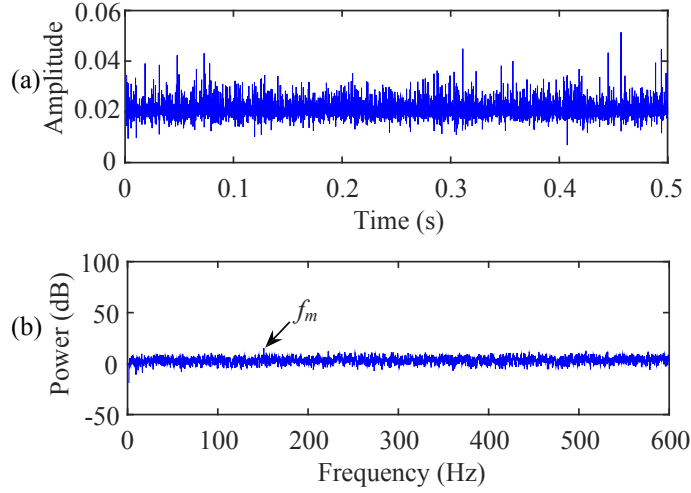
Figure 4.5. (a) TKE of the simulated AM signal, (b) the corresponding frequency spectrum.

The magnitude of the modulating frequency in the spectrum can be highlighted by using the GTKE using an optimal lag for the given modulating frequency f_m. By using an itinerary process, the GTKE technique is applied to the simulated signal with different lag k. The optimal lag will generate a spectrum where the amplitude of the modulating frequency is enhanced against the background noise. This itinerary procedure can be mathematically expressed as

$$\overline{k}_{f_m} = \arg_{(k)} \max \left\{ P_{\Psi_k}(f = f_m) \right\} \tag{4.16}$$

where P_{Ψ_k} is the frequency spectrum of GTKE and $\overline{k}_{f_m}$ is the optimal lag for the given f_m. Figure 4.6 illustrates the results of the itinerary process. Classical TKE corresponding to $k = 1$ is the worst in this case for the noise reduction with the lowest dB enhancement. The optimal lag is at $\overline{k}_{f_m} =$ 20. Figure 4.7 shows the time domain representation of the optimized GTKE. The modulating frequency is the dominating spectral component, indicating that the optimized GTKE technique can effectively recognize the modulating frequency for the signal with additive noise.

51
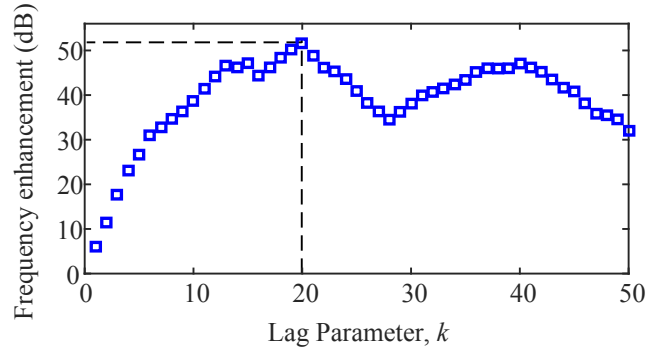
Figure 4.6. The frequency enhancement of the modulating frequency in the frequency spectrum of GTKE for different k values.

Figure 4.7. (a) The optimized GTKE of the simulated AM signal, (b) the corresponding frequency spectrum.

Another AM signal is simulated for the different modulating frequency between 100 Hz and 400 Hz to determine $\overline{k}_{f_m}$ using the same itinerary approach as discussed before. The objective is to enhance the spectral amplitude of each f_m. Figure 4.8 illustrates the resulting frequency spectrum corresponding to the simulations for f_m: $f_m = 100$ Hz, 200 Hz, and 300 Hz. The frequency spectra of the classical TKE with $k = 1$ have the lowest SNR due to the noise sensitivity, as depicted in Figure 4.8(a,b,c). Figure 4.8(d,e,f) present the resulting spectra of GTKEs with non-optimized lags, those the SNR is improved compared to the classical TKE when $k = 1$. The corresponding

optimized GTKE results with maximum enhancement of the modulation frequency are illustrated in Figure 4.8(g,h,i).
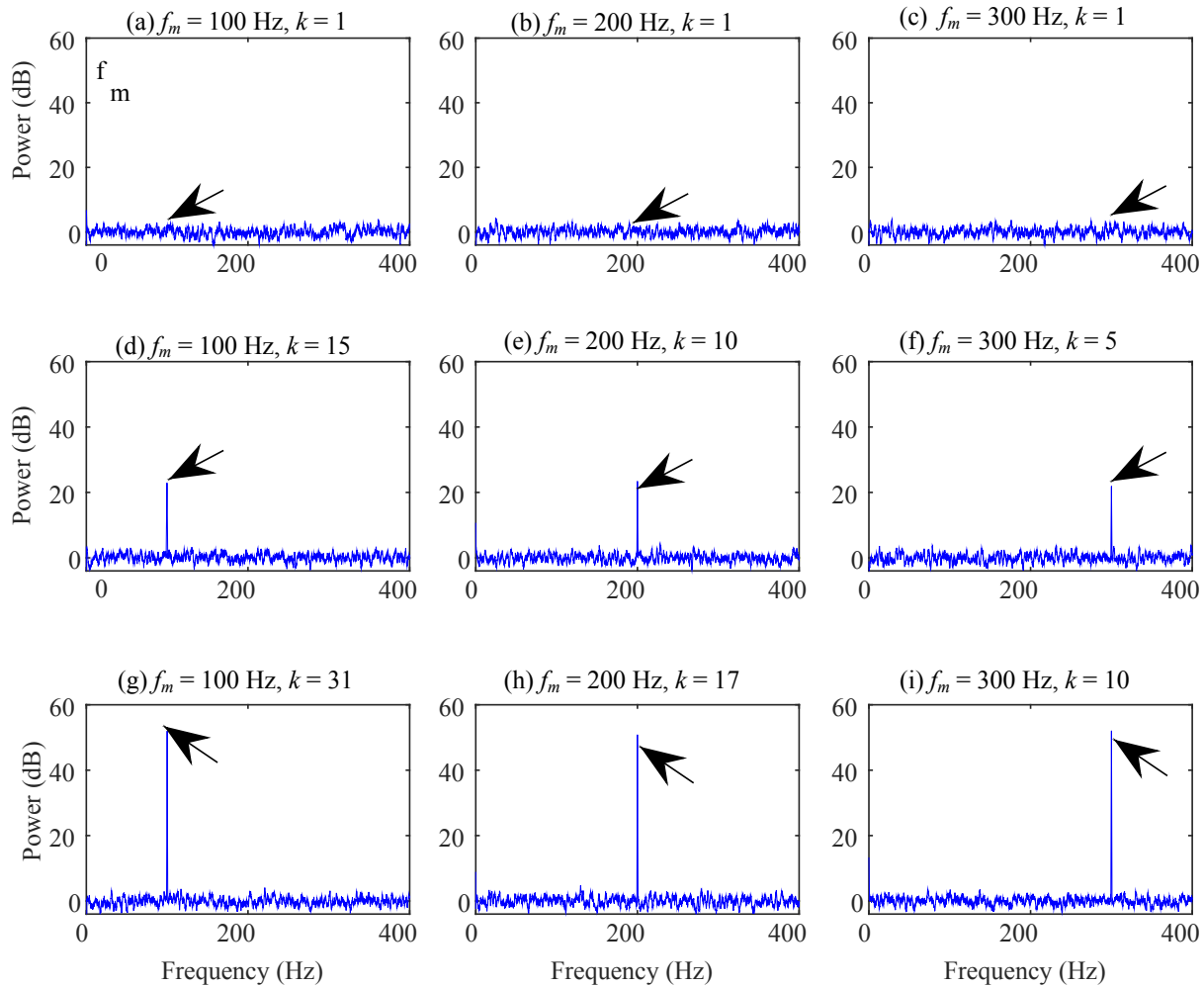
Figure 4.8. Frequency spectra of the GTKEs calculated by different lag k for three AM signal simulations.

Figure 4.9 shows the results of GTKE technique with optimization tests for modulation frequencies from 100Hz to 400 Hz. In comparison with the results in Figure 4.8, it is seen that there is a correlation between the modulation frequency and the corresponding lag k. Based on the simulation results, a mathematical expression for an optimal lag to maximize the modulating frequency component against noise will be computed as

$$\bar{k} = \frac{f_s}{2f_m} \tag{4.17}$$

where f_s is the sampling frequency. Figure 4.9 depicts the generated theoretical optimal lag parameter from Equation (4.17).
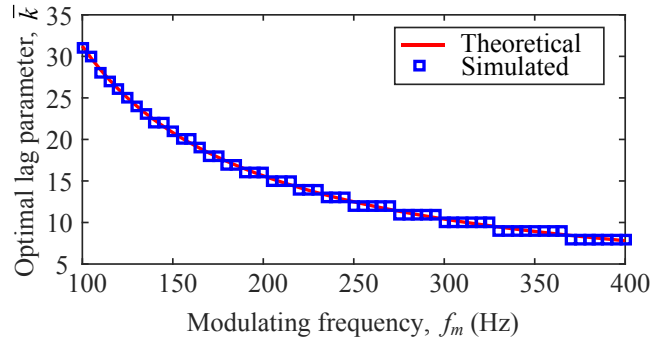
Figure 4.9. The simulation results for GTKE technique optimization for signals with different modulation frequencies. The simulation results are depicted with the blue squares and the red line represents the generated theoretical value, based on Equation (4.17).

If the same tests are conducted for the AM signal with a carrier frequency lower than the modulating frequency, or $f_m > f_c$, the dataset information of the simulated signal is summarized in Table 4.3. Figure 4.10 shows AM signal in its time domain and frequency domain representations. Since the modulated frequency is higher than the carrier frequency, the sidebands occupy higher frequency bandwidths than f_c. However, the sidebands are masked by the noise in this case. Figure 4.11 shows processing results of the TKE operator, where the modulating frequency is masked by the background noise.

Table 4.3. AM signal simulation parameters for $f_m > f_c$.

f_m	f_c	κ	A	f_s	N	σ_{noise}
150 Hz	50 Hz	0.03	1	6247 Hz	16000	0.3
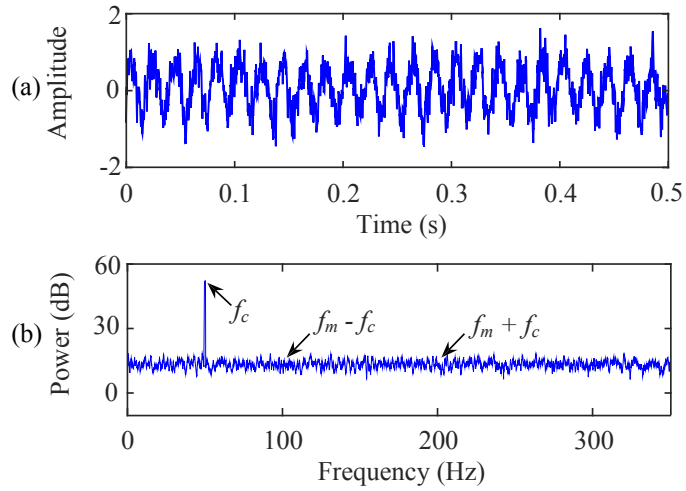
Figure 4.10. (a) The simulated AM signal with additive Gaussian noise, (b) the corresponding frequency spectrum.
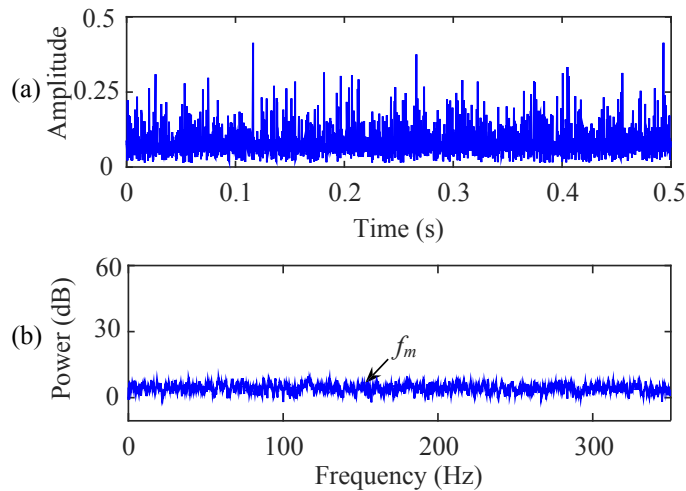
Figure 4.11. (a) The TKE of the simulated AM signal, (b) the corresponding frequency spectrum.

Figure 4.12 shows the processing results by the use of the proposed GTKE technique; the optimal parameter is $\bar{k}_{f_m}$ = 40. Similarly, the TKE corresponding to k = 1 has the worst performance in enhancing the modulation frequency component against noise.
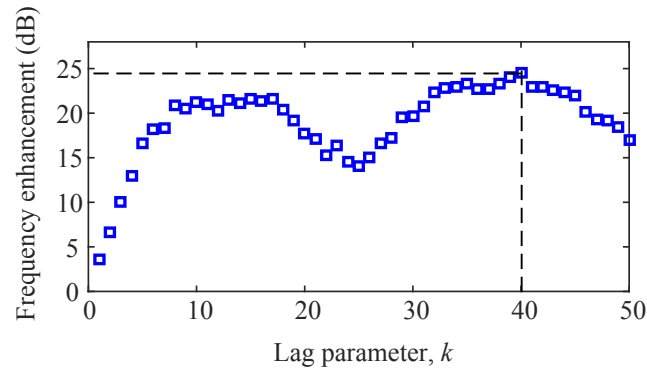
Figure 4.12. The frequency enhancement of the modulating frequency in the GTKE for different k values.

The GTKE and the corresponding frequency spectra of the signal are illustrated in Figure 4.10. The optimized GTKE technique can successfully recognize the modulation signal buried in noise.
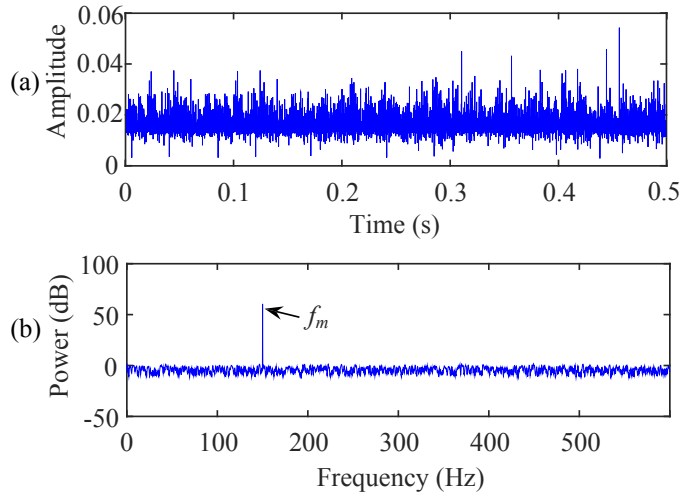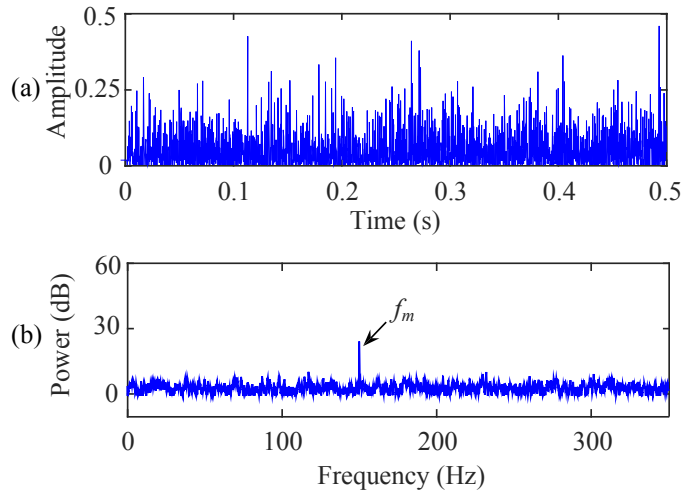
Figure 4.13. (a) The optimized GTKE of the simulated AM signal, (b) the corresponding frequency spectrum.

For AM signals with modulating frequency over [100, 400] Hz, the optimal lag is calculated and shown in Figure 4.14. The theoretical optimal lag that maximizes the modulating frequency is represented with the red line, and will be calculated as

$$\bar{k} = \frac{f_s}{f_m} \tag{4.18}$$
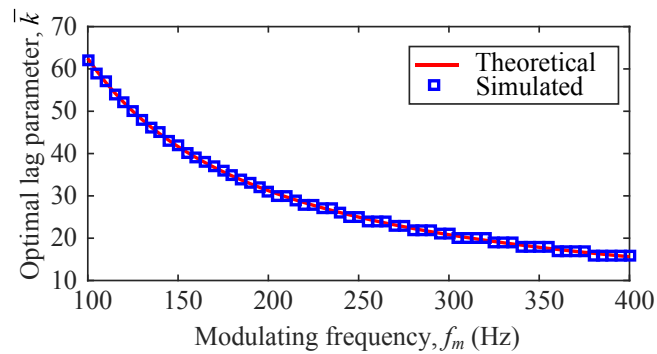
Figure 4.14. (a) The optimized GTKE of the simulated AM signal, (b) the corresponding frequency spectrum.

In summary, for an AM signal, the optimal lag $\overline{k}_{f_m}$ for the GTKE technique can be calculated as

$$\overline{k}_{f_m} = \begin{cases} \left\langle \dfrac{f_s}{2f_m} \right\rangle & f_m < f_c \\[3ex] \left\langle \dfrac{f_s}{f_m} \right\rangle & f_m > f_c \end{cases} \qquad (4.19)$$

Chapter 5 Experimental Tests and Results

The proposed GTKE technique is implemented to detect closely spaced frequency components. The effectiveness of GTKE-based signal demodulation against noise will be investigated experimentally in this chapter corresponding to different IM conditions. It will be stated that the proposed WSS is a comprehensive DAQ system, consisting of many units. Several challenging issues have been solved in Chapter 3, including low power consumption, consistent data sampling and reliable wireless communication. Although the developed WSS system has reached the capability for fundamental DAQ operations, it still has some limitations to be implemented for large number of data acquisition in real applications due to reasons such as SRAM space limitations, consistency of the data sampling time due to the SRAM and MCU communication, and wireless communication speed. Correspondingly, in this test, an existing wired DAQ board is used for data collection, to take advantage of the 12-bit ADC resolution instead of the 10-bit ADC in the developed WSS system.

5.1 Experimental Setup

Figure 5.1 shows the exprimental setup used in this testing. The tested IM is three-phase, 50 Hz supply frequency, squirrel cage, 1/3-hp motor (by Marathon Electric). The shaft speed of the motor is controlled by a VFD speed controlling system (VFD-B by Delta Electronics) with a speed range of 1 - 400 Hz. The external load is applied by a high torque magnetic particles clutch (PHC-50 by Placid Industries) with a torque range of 1.3-40 Nm. The load level of the magnetic clutch is controlled by a constant current source. The shaft speed ratio is adjusted for the load system by a gearbox (Gear 800 by Boston Gear) to safely operate the load system. An analog accelerometer (ICP 603C01 by IMI Sensors) is mounted over the IM with a magnet to track the shaft rotation speed and to collect the vibration data with a measurement range of ±50 g and a frequency range from 0.5 Hz to 10000 Hz. The stator current signals in three phases are measured by using three analog hall effect current transducers (LTS 6-NP). The DAQ board (Quanser Q4) with four analog inputs and 12-bit ADC is used for the vibration and stator current detection.
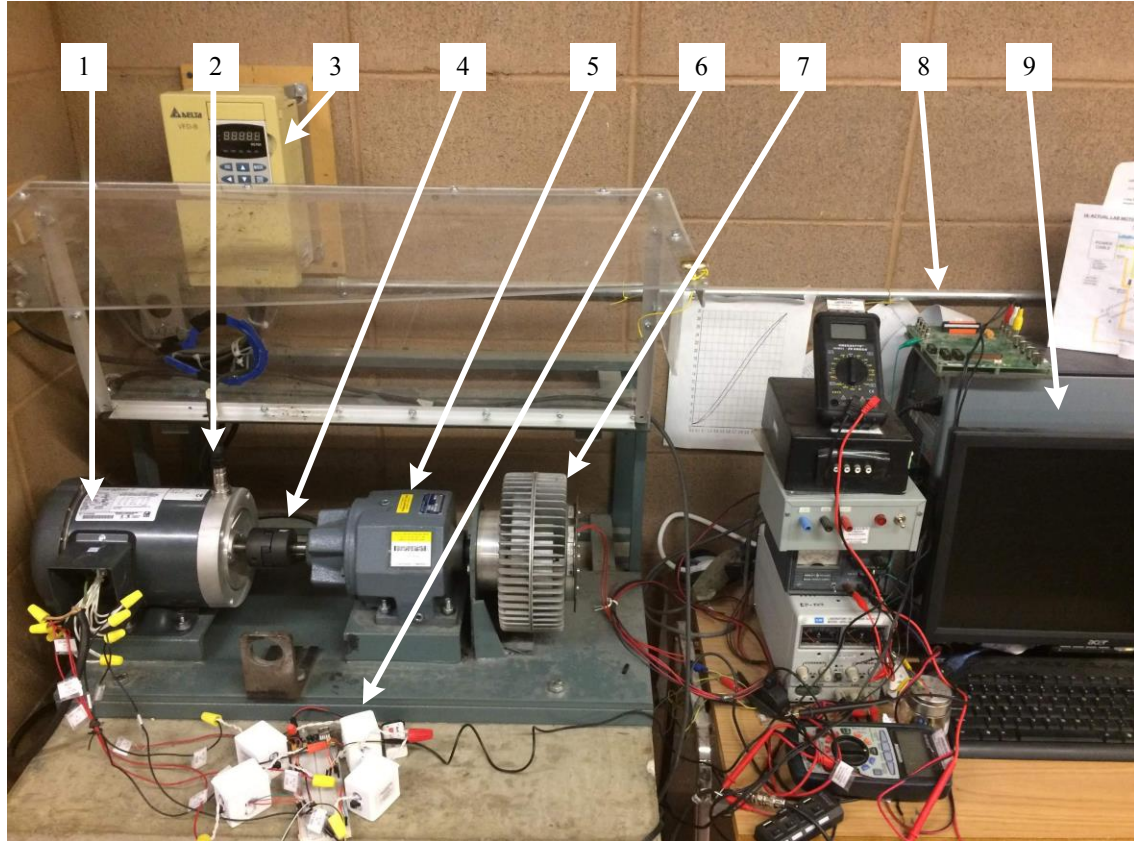
Figure 5.1. IM experimental setup. 1 – Tested IM, 2 – ICP acceleration sensor, 3 – VFD speed controlling, 4 – Clutch, 5 – Gearbox, 6 – Hall effect current sensors, 7 – Load system, 8 – DAQ system, 9 – Computer.

Two ball bearings are connected to the IM shaft. A healthy bearing is installed at the fan-end of the IM. A 0.02 inch hole is drilled through the outer race of the drive-end bearing to simulate a localized outer race defect, as illustrated in Figure 5.2. The deep groove ball bearings are NSK6203 with a pitch diameter $D = 28.7$ mm, ball diameter $d = 6.747$ mm and number of balls $N = 8$. The contact angle $\theta = 0°$ in theory. The corresponding fault characteristic frequency is calculated to be $f_v = 3.053 f_r$ based on the bearing geometry according to Equation (3.10).
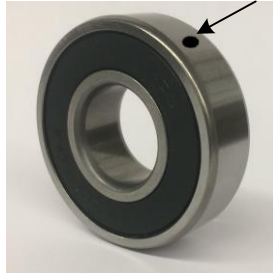
Figure 5.2. A representative picture of a ball bearing with an artificially introduced outer race defect.

5.2 Vibration-based Bearing Fault Detection

Firstly, the vibration signal is used for analysis. The motor is tested under three different supply frequencies f_e: 35 Hz, 50 Hz, and 60 Hz. For each condition, the motor is tested under four load conditions: no load (IM is decoupled from the load system), low load (approximately 30% of the rated power), medium load (approximately 60% of the rated power) and heavy load (approximately 90% of the rated power) based on the slip. The vibration data is collected from a healthy motor (with healthy bearings) and a motor with an outer race bearing defect. The default sampling frequency of the DAQ system at f_s = 6450 Hz is selected. Figure 5.3 shows part of the vibration signal collected at 50 Hz supply frequency and low load. Because the background noise masks the fault-related impulses, it is difficult to predict the health conditions of the IM bearings on the time signals of the vibration.
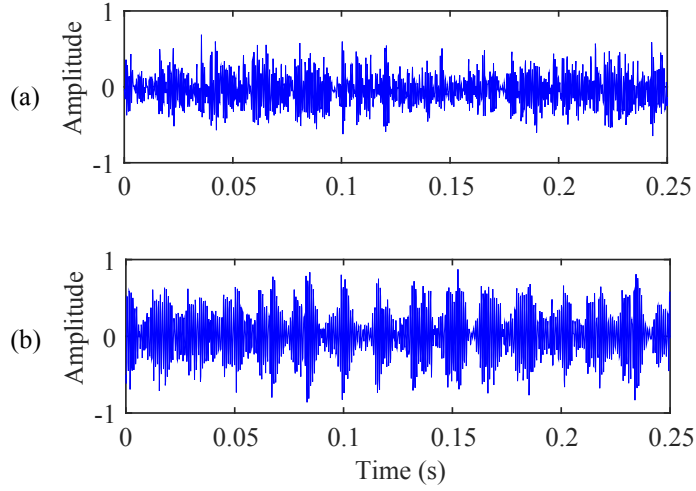
Figure 5.3. Part of vibration signal for IMs at 50 Hz supply frequency and low load, (a) Healthy IM, (b) IM with an outer race bearing defect.

To examine the effectiveness of the proposed GTKE technique, the Hilbert transform-based envelope analysis, and the TKE spectrum technique are implemented for comparison. For each load level and supply frequency, the vibration data of the healthy motor and the motor with faulty bearing is processed using the related signal processing techniques to examine the characteristic frequency components. Hanning window is used to reduce the leakage in spectral analysis. The spectrums are normalized in terms of the amplitude of the maximum spectral component to facilitate comparison analysis between the spectrums:

$$F_{norm}\left(x_v[n]\right) = \frac{\left|F\left(x_v[n]\right)\right|}{\max\left\{\left|F\left(x_v[n]\right)\right|\right\}} \tag{5.1}$$

where $F(x_v[n])$ is the spectral function of the discrete vibration signal $x_v[n]$ using the Fourier transform. Correspondingly, the spectral amplitude will take values between [0-1].

Figure 5.4 illustrates the implementation of the proposed technique for IM bearing fault detection. For each dataset, $N = 100,000$ data points are collected. The optimization of the GTKE technique is carried out by initially investigating the TKE spectrum of the signal to obtain the shaft

62

speed. Based on the shaft frequency, the expected characteristic fault frequency f_v and the corresponding optimal lag $\bar{k}_{f_m}$ are calculated.
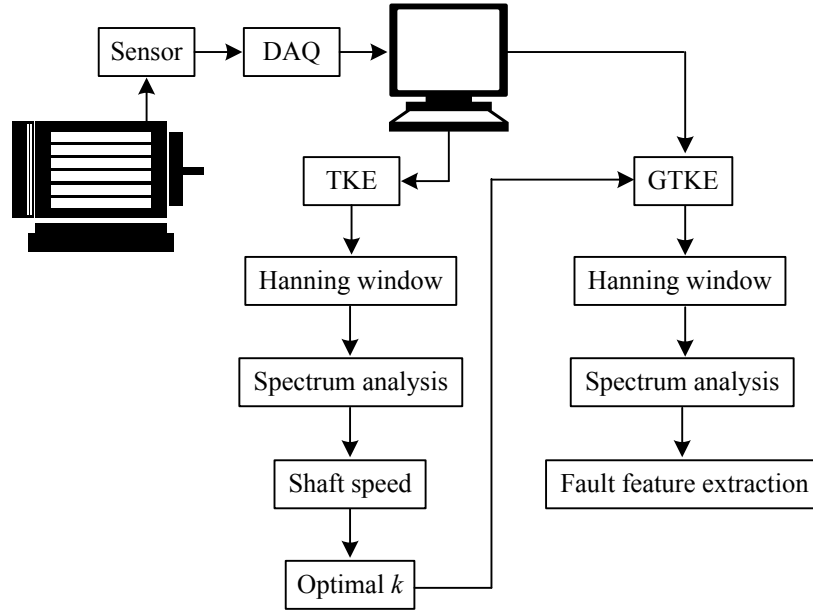
Figure 5.4. Schematic of the IM bearing condition monitoring.

5.2.1 Supply Frequency 35 Hz

Firstly, these two IMs are tested under no load condition, with the magnetic load clutch being disconnected from the shaft of the IM. Figure 5.5 shows the processing results using the related techniques. The shaft speed $f_r = 35$ Hz dominates the spectrums. The characteristic frequency is calculated as $f_v = 106.8$ Hz. The optimal lag for the GTKE technique is calculated as $\bar{k} = 29$. Figure 5.5(a,b) illustrate the processing results using Hilbert based envelope analysis for the tested IMs. The characteristic frequency can be detected in the IM with the bearing defect, as shown in Figure 5.5(b). Figure 5.5(c,d) shows the TKE technique results. The two motors are not distinguishable as the characteristic frequency is not present in either case. It is seen from Figure 5.5(e,f) that the proposed GTKE technque can recognize the bearing characteristic frequency f_v using optimized lag, even though it is not the dominant spectral component.

Figure 5.5. The processing results for IMs with a healthy bearing (a,c,e) and a faulty bearing (b,d,f) at 35 Hz supply frequency and no load, (a, b) Hilbert based envelope analysis, (c, d) TKE technique, (e, f) Proposed GTKE technique Red arrows indicate the shaft speed frequency; black arrows indicate the bearing characteristic frequency).

The IMs are then tested under low load condition.

Figure 5.6 presents the result, with the characteristic frequency $f_v = 105.6$ Hz, and optimal lag parameter $\bar{k} = 29$. Although all three techniques can detect the fault in this case, the proposed GTKE technique outperforms the others in enhancing the fault related feature as the characteristic fault frequency component dominates the spectral map.

Figure 5.6. The processing results for IMs with a healthy bearing (a,c,e) and a faulty bearing (b,d,f) at 35 Hz supply frequency and full load, (a, b) Hilbert based envelope analysis, (c, d) TKE technique, (e, f) Proposed GTKE technique. (Red arrows indicate the shaft speed frequency; black arrows indicate the bearing characteristic frequency).

5.2.2 Supply Frequency 50 Hz

The fault detection techniques are tested with a supply frequency f_v = 50 Hz under different load levels. Firstly, the IMs are operated with no external load. Figure 5.7 shows the processing results using the related techniques. The shaft speed can be estimated by examining the envelope spectrums. The characteristic frequency is calculated as f_v = 152.49 Hz in this case and the optimal lag for the proposed GTKE technique is $\bar{k}$ = 20. Figure 5.7(a,b) illustrates the processing results of the IMs using Hilbert based envelope analysis. Although, the bearing characteristic frequency is present in the spectrum, the amplitude of the related spectral component is low. In Figure 5.7(d), the TKE technique fails to clearly recognize the characteristic features to predict the health conditions of the IM with the outer race bearing defect. The optimized GTKE technique can

enhance the characteristic features in Figure 5.7(f) to diagnose the IM with a bearing fault, which outperforms other two techniques when the spectral amplitudes are compared.

Figure 5.7. The processing results for IMs with a healthy bearing (a,c,e) and a faulty bearing (b,d,f) at 50 Hz supply frequency and no load, (a, b) Hilbert based envelope analysis, (c, d) TKE technique, (e, f) Proposed GTKE technique Red arrows indicate the shaft speed frequency; black arrows indicate the bearing characteristic frequency).

The motor is then tested under low load. The characteristic frequency is $f_v = 152.1$ Hz. The optimal lag for the GTKE technique is $\bar{k} = 20$. As illustrated in Figure 5.8, all three techniques can recognize the characteristic frequency components from the envelope spectrums of the faulted motors. But the proposed GTKE technique outperforms the other two techniques as the fault frequency dominates spectral map in Figure 5.8(f).
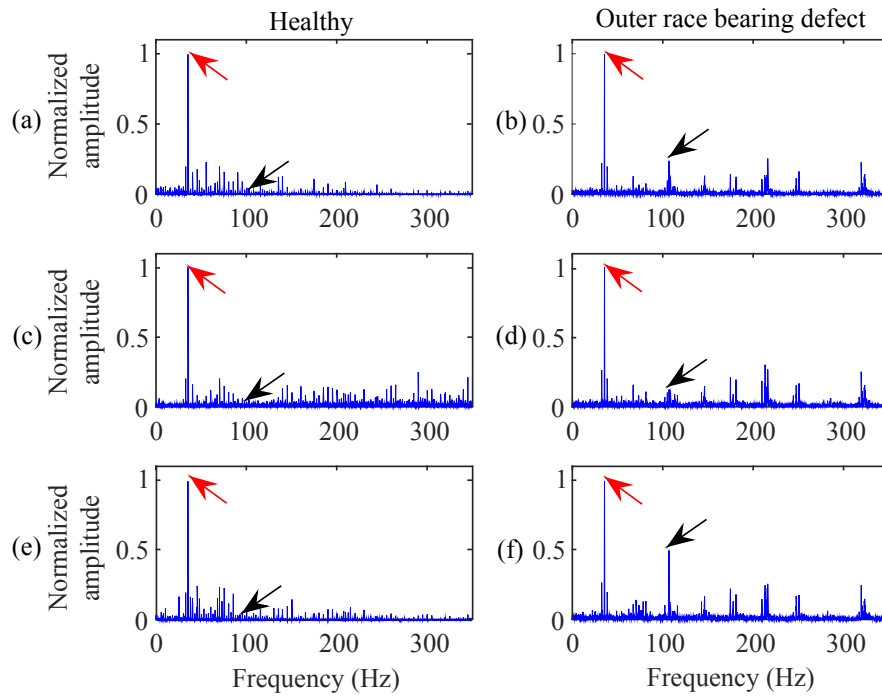
66

Figure 5.8. The processing results for IMs with a healthy bearing (a,c,e) and a faulty bearing (b,d,f) at 50 Hz supply frequency and low load, (a, b) Hilbert based envelope analysis, (c, d) TKE technique, (e, f) Proposed GTKE technique. (Red arrows indicate the shaft speed frequency; black arrows indicate the bearing characteristic frequency).

Figure 5.9 shows the processing results of the IMs tested under medium load state. The characteristic frequency is $f_v = 151.2$ Hz. The optimal lag is $\bar{k} = 20$. Although the vibration signals from the IM with a faulty bearing has lower SNR than the healthy IM, both the Hilbert based envelope analysis and GTKE technique can recognize the characteristic fault frequency clearly, but the GTKE has better resolution as the fault feature dominates its spectral map in Figure 5.9(f).
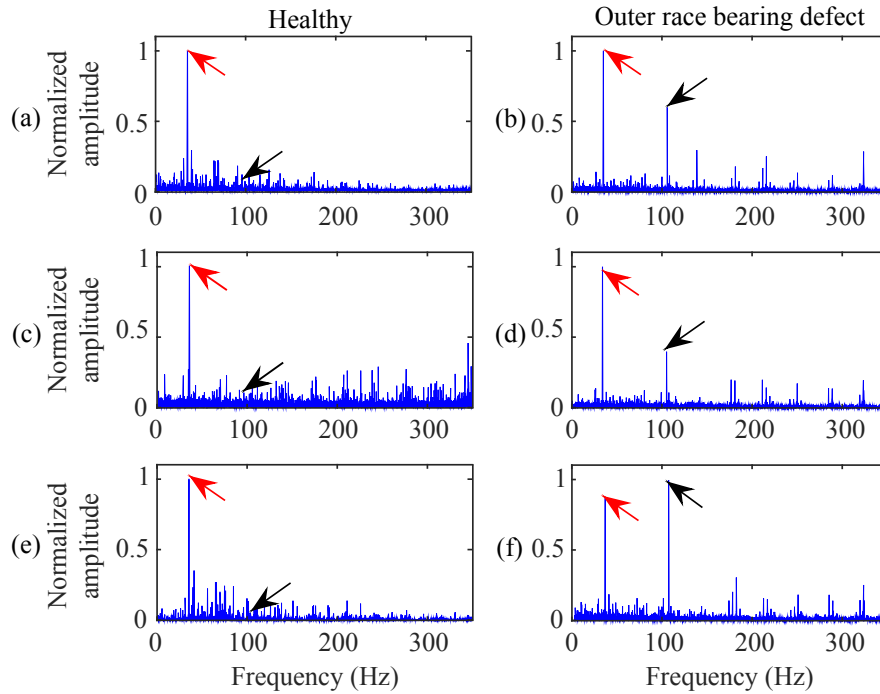
Figure 5.9. The processing results for IMs with a healthy bearing (a,c,e) and a faulty bearing (b,d,f) at 50 Hz supply frequency and medium load, (a, b) Hilbert based envelope analysis, (c, d) TKE technique, (e, f) Proposed GTKE technique. (Red arrows indicate the shaft speed frequency; black arrows indicate the bearing characteristic frequency).

Figure 5.10 shows the processing results of the related techniques under a full load level; the characteristic frequency is f_v = 150.9 Hz in this case, and the optimal lag for the GTKE technique is $\overline{k}$ = 20. Similarly, both Hilbert based envelope analysis (Figure 5.10(b)) and GTKE technique (Figure 5.10(f)), can recognize the bearing fault. Under full load, the Hilbert based envelope technique also can recognize the second harmonic of the characteristic frequency.
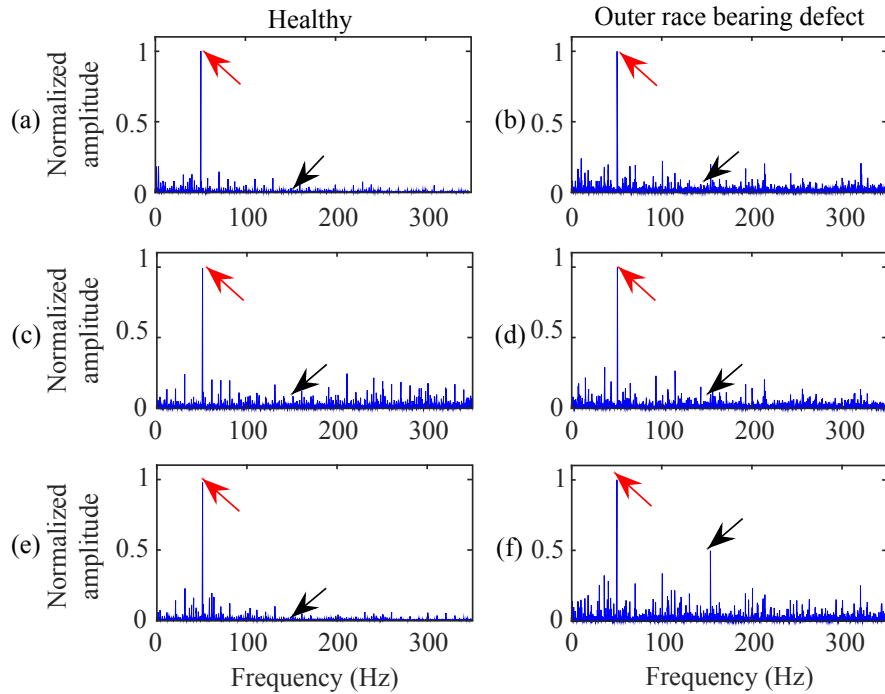
Figure 5.10. The processing results for IMs with a healthy bearing (a,c,e) and a faulty bearing (b,d,f) at 50 Hz supply frequency and full load, (a, b) Hilbert based envelope analysis, (c, d) TKE technique, (e, f) Proposed GTKE technique. (Red arrows indicate the shaft speed frequency; black arrows indicate the bearing characteristic frequency).

5.2.3 Supply Frequency 60 Hz

Two IMs with healthy bearings and a bearing with an outer race defect are tested with 60 Hz supply frequency under four load levels. Firstly, with no load, Figure 5.11 shows the analysis results. The characteristic frequency is f_v = 182.9 Hz in this case, and the optimal lag for the GTKE technique is $\bar{k}$ = 18. In this case, the optimized GTKE in Figure 5.11 is the only technique that can detect the bearing fault, even though the characteristic frequency does not dominate the spectrum.
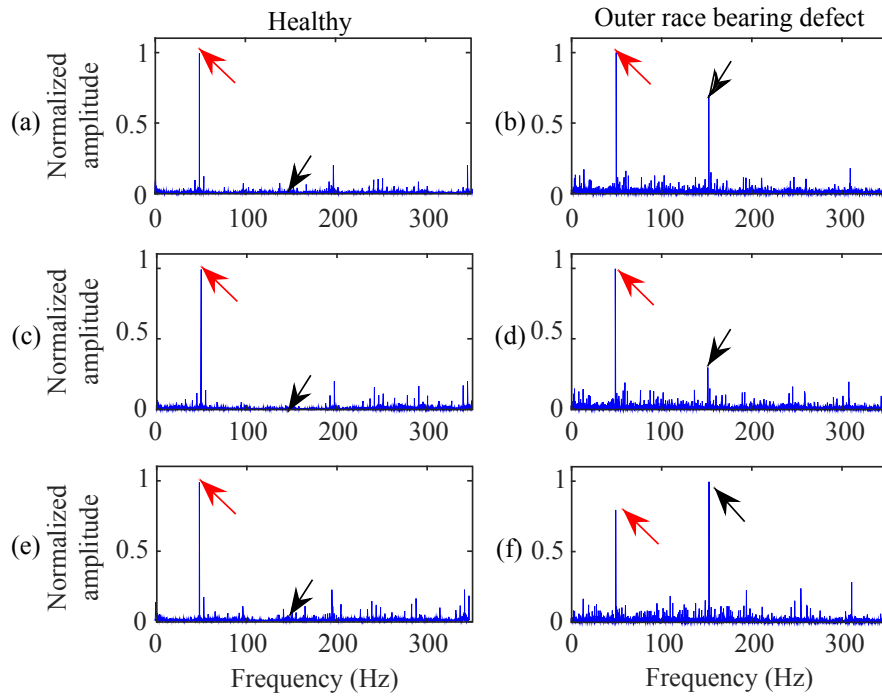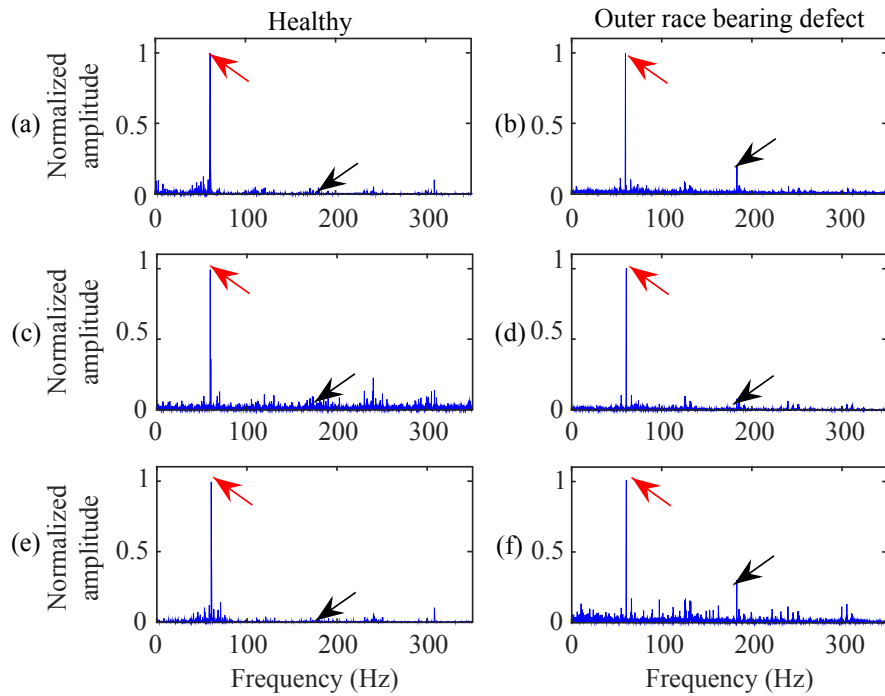
Figure 5.11. The processing results for IMs with a healthy bearing (a,c,e) and a faulty bearing (b,d,f) at 60 Hz supply frequency and no load, (a, b) Hilbert based envelope analysis, (c, d) TKE technique, (e, f) Proposed GTKE technique. (Red arrows indicate the shaft speed frequency; black arrows indicate the bearing characteristic frequency).

Figure 5.12 shows the processing results with low load and a supply frequency of 60 Hz. The characteristic frequency is $f_v = 181.32$ Hz, and $\bar{k} = 18$. All of these three techniques can diagnose the healthy motor clearly. The proposed GTKE technique outperforms other two methods for IM bearing fault detection with higher resolution.
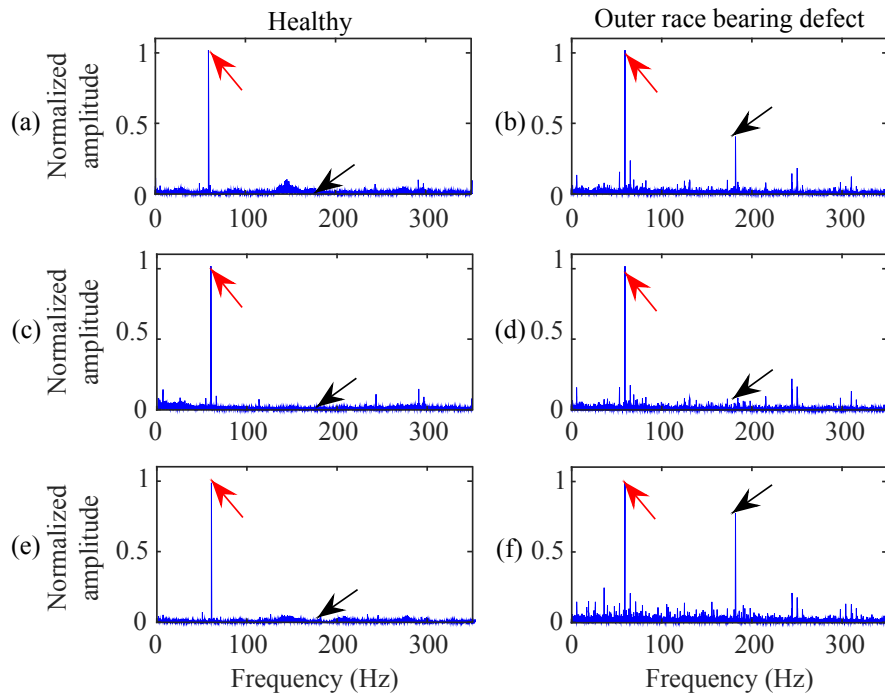
Figure 5.12. The processing results for IMs with a healthy bearing (a,c,e) and a faulty bearing (b,d,f) at 60 Hz supply frequency and low load, (a, b) Hilbert based envelope analysis, (c, d) TKE technique, (e, f) Proposed GTKE technique. (Red arrows indicate the shaft speed frequency; black arrows indicate the bearing characteristic frequency).

Figure 5.12 shows the processing results under medium load with $f_v = 179.98$ Hz and $\bar{k} = 17$. In this case, the proposed GTKE technique can clearly recognize the IM bearing defect with a dominant spectral component.
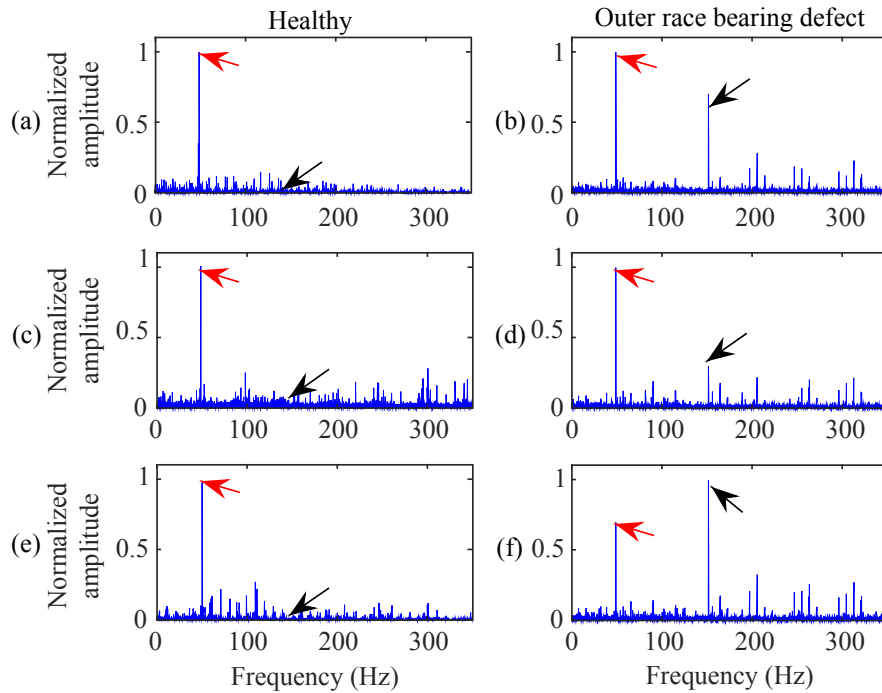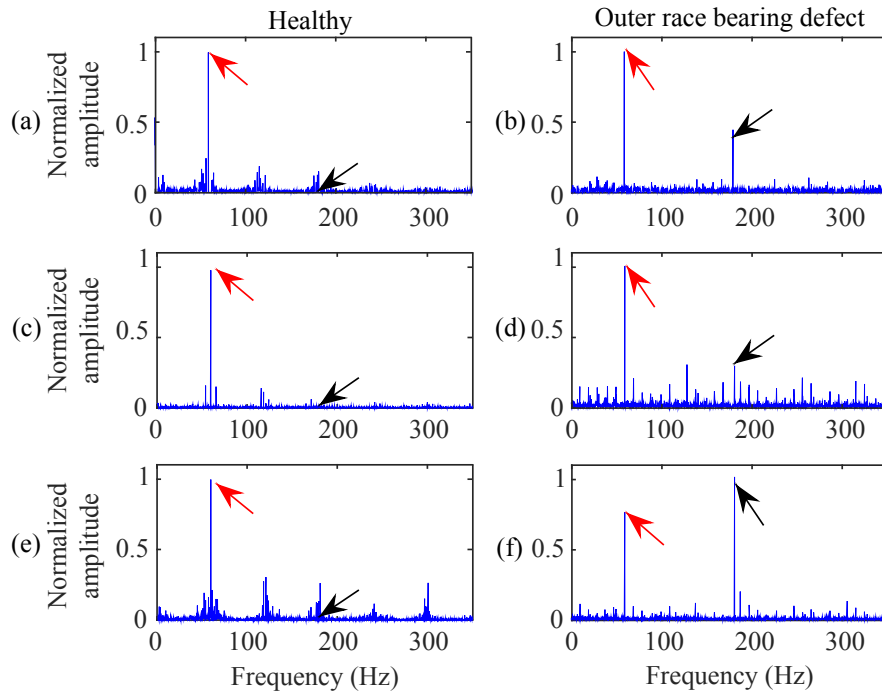
Figure 5.13. The processing results for IMs with a healthy bearing (a,c,e) and a faulty bearing (b,d,f) at 60 Hz supply frequency and medium load, (a, b) Hilbert based envelope analysis, (c, d) TKE technique, (e, f) Proposed GTKE technique. (Red arrows indicate the shaft speed frequency; black arrows indicate the bearing characteristic frequency).

Figure 5.14 shows the processing results for the IMs with high load condition. The characteristic frequency is fv = 179.98 Hz and $\bar{k}$ = 35. Both the Hilbert based envelope analysis and the GTKE techniques can provide clearly diagnostic results in this case.
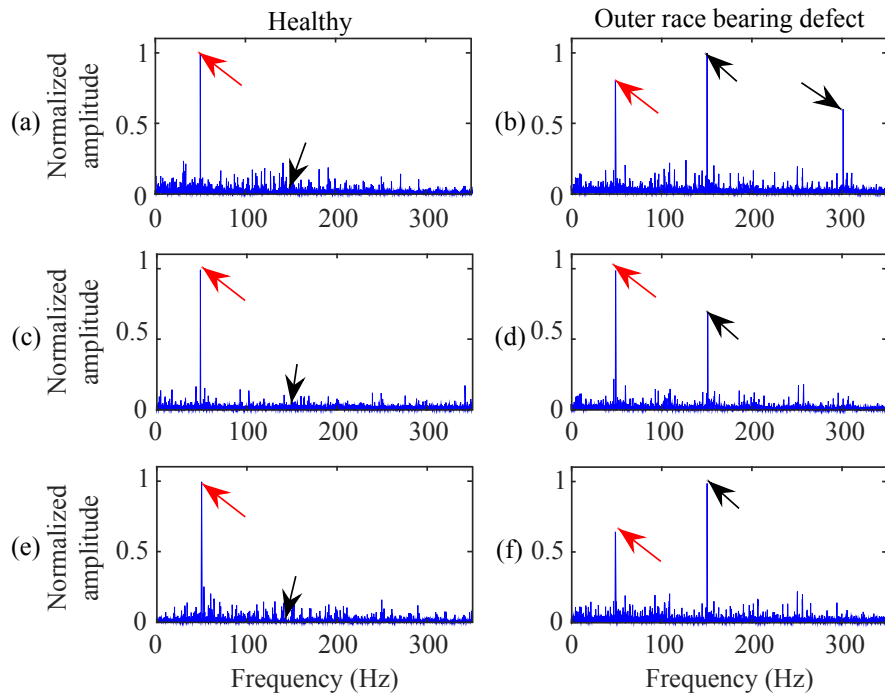
Figure 5.14. The processing results for IMs with a healthy bearing (a,c,e) and a faulty bearing (b,d,f) at 60 Hz supply frequency and full load, (a, b) Hilbert based envelope analysis, (c, d) TKE technique, (e, f) Proposed GTKE technique. (Red arrows indicate the shaft speed frequency; black arrows indicate the bearing characteristic frequency).

5.3 Current-based Bearing Fault Detection

Unlike the vibration signals, which consist of frequency components with relatively closer energy levels, the supply frequency harmonic of the stator current is in orders of magnitude stronger than the other frequency components. Correspondingly, a decibel representation of the spectral amplitudes is more appropriate for stator current representation, such that

$$P\left(x_c[n]\right) = 20\log_{10}\left(\frac{1}{N}\left|F\left(x_c[n]\right)\right|^2\right) \tag{5.2}$$

73

where $F(x_c[n])$ is the frequency spectrum of the signal obtained by FFT, N is the length of the discrete current signal $x_c[n]$.
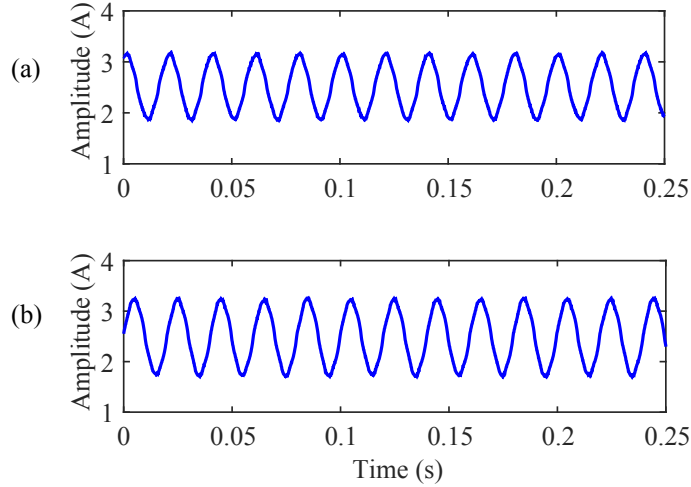
Figure 5.15. Part of collected stator current signal for IMs at 50 Hz supply frequency and low load, (a) Healthy motor, (b) motor with an outer race bearing defect.

The stator current signals for the testing are collected simultaneously with the vibration data of the previous tests. For each condition, the shaft rotation speeds and the characteristic frequencies remain the same. As previously mentioned, a preliminary investigation of the Hilbert based envelope analysis of the vibration signal can present the shaft rotation speed. The data processing is carried out off-line using MATLAB. Each signal consists of $N = 100,000$ data points with the default sampling frequency of the DAQ system $f_s = 6247$ Hz. Figure 5.15 shows the parts of the collected stator current signals for these two motors. As can be seen, it is difficult to recognize the differences between the current signatures from two IMs.

To test the effectiveness of the proposed GTKE technique, the stator current signals from a health IM and a IM with a bearing defect are collected under different supply frequencies and load conditions. For each condition, three techniques (Hilbert based envelope analysis, TKE technique and the proposed GTKE technique) are tested for effectiveness comparison in IM bearing fault detection.

5.3.1 Supply Frequency 35 Hz

Figure 5.16 shows the processing results for the IMs with no external load. The characteristic fault frequency is $f_c = 106.8$ Hz in this case. The proposed GTKE technique is the only technique that can recognize the faulty characteristic frequency, even though it is still very weak. Advanced filtering techniques can be implemented to improve SNR.
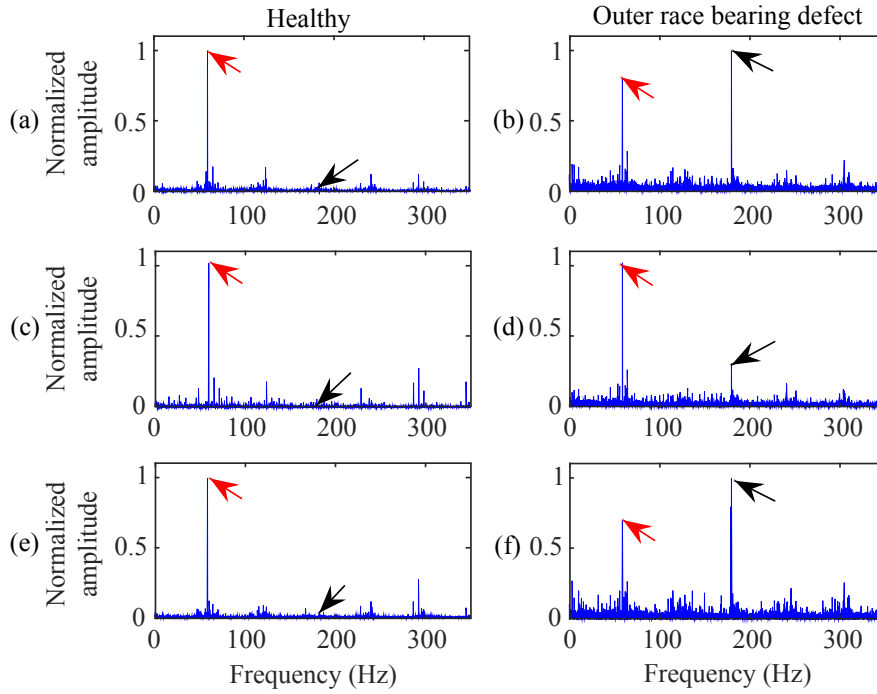

Figure 5.16. The processing results for IMs with a healthy bearing (a,c,e) and a faulty bearing (b,d,f) at 35 Hz supply frequency and no load, (a, b) Hilbert based envelope analysis, (c, d) TKE technique, (e, f) Proposed GTKE technique. (Red arrows indicate the shaft speed frequency; black arrows indicate the bearing characteristic frequency).

Figure 5.17 shows the processing results of the motors with low load. The proposed GTKE technique can detect the characteristic fault frequency at $f_c = 105.6$ Hz with a relatively higher resolution, even though the features are weak.

Figure 5.17. The processing results for IMs with a healthy bearing (a,c,e) and a faulty bearing (b,d,f) at 35 Hz supply frequency and full load, (a, b) Hilbert based envelope analysis, (c, d) TKE technique, (e, f) Proposed GTKE technique. (Red arrows indicate the shaft speed frequency; black arrows indicate the bearing characteristic frequency).

5.3.2 50 Hz Supply Frequency

Figure 5.18 shows the processing results with no external load. Similarly, the GTKE technique is the only method that can recognize the weak characteristic frequency in Figure 5.18. However, the fault-related features are weak and cannot be used reliably for IM bearing fault detection due to the low SNR. This is due to the fact that when the there is no external load on the rotor shaft, rotor slid is very small, it is difficult to demodulate irregular features related to bearing defects.

Figure 5.18. The processing results for IMs with a healthy bearing (a,c,e) and a faulty bearing (b,d,f) at 50 Hz supply frequency and no load, (a, b) Hilbert based envelope analysis, (c, d) TKE technique, (e, f) Proposed GTKE technique. (Red arrows indicate the shaft speed frequency; black arrows indicate the bearing characteristic frequency).

Figure 5.19 shows the processing results using the stator current for low load condition. The characteristic frequency components are visible in all three envelope spectrums. However, the proposed GTKE outperforms another two techniques as it can enhance the power of the fault-related information.

Figure 5.19. The processing results for IMs with a healthy bearing (a,c,e) and a faulty bearing (b,d,f) at 50 Hz supply frequency and low load, (a, b) Hilbert based envelope analysis, (c, d) TKE technique, (e, f) Proposed GTKE technique. (Red arrows indicate the shaft speed frequency; black arrows indicate the bearing characteristic frequency).

The processing results for the IM with a bearing fault for a medium and a full load level are shown in Figure 5.20 and Figure 5.21, respectively. It is seen that in these case, the GTKE is the only technique that can recognize the bearing defect due to his capability in enhancing the power of the fault-related frequency component.
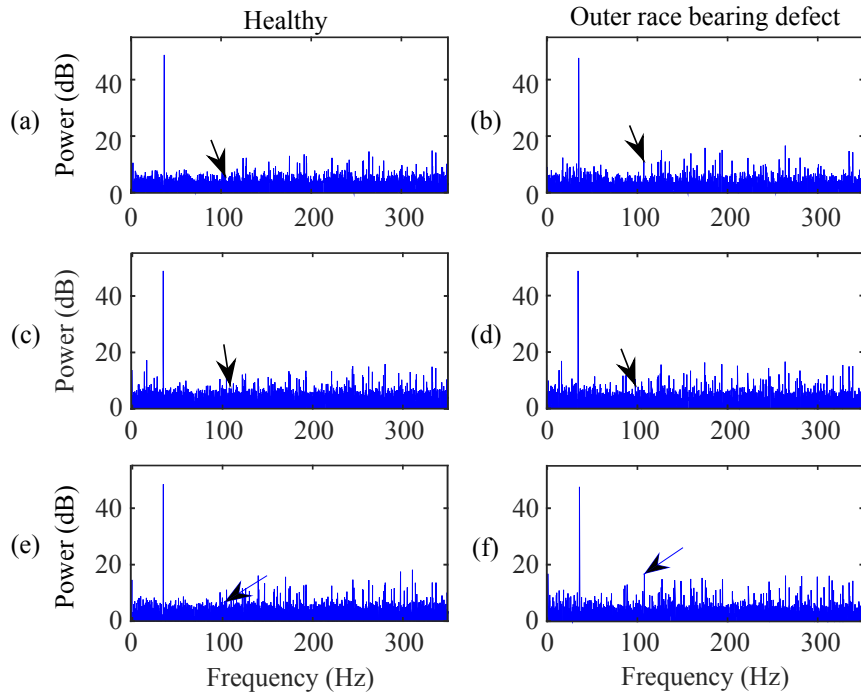
Figure 5.20. The processing results for IMs with a healthy bearing (a,c,e) and a faulty bearing (b,d,f) at 50 Hz supply frequency and medium load, (a, b) Hilbert based envelope analysis, (c, d) TKE technique, (e, f) Proposed GTKE technique. (Red arrows indicate the shaft speed frequency; black arrows indicate the bearing characteristic frequency).
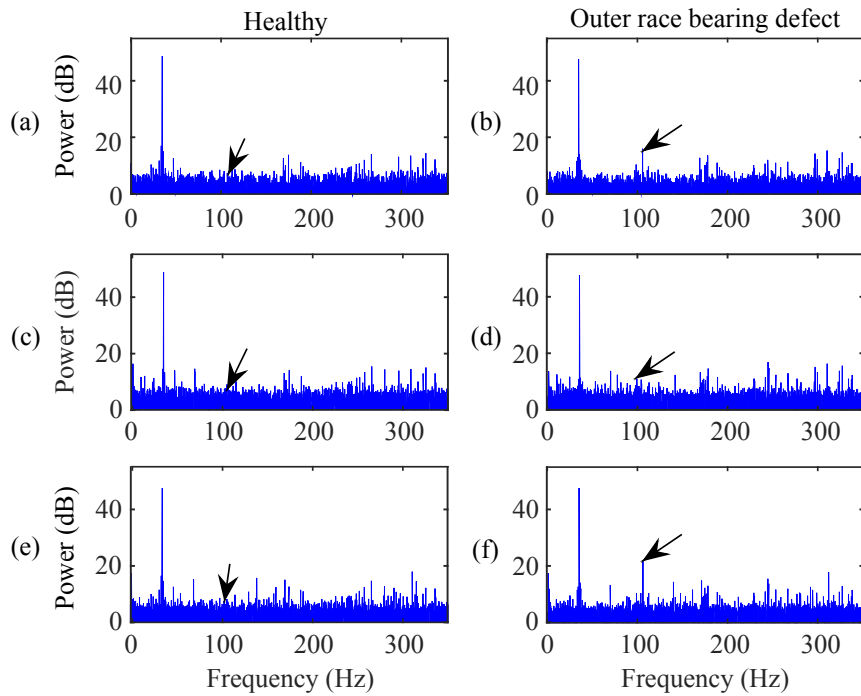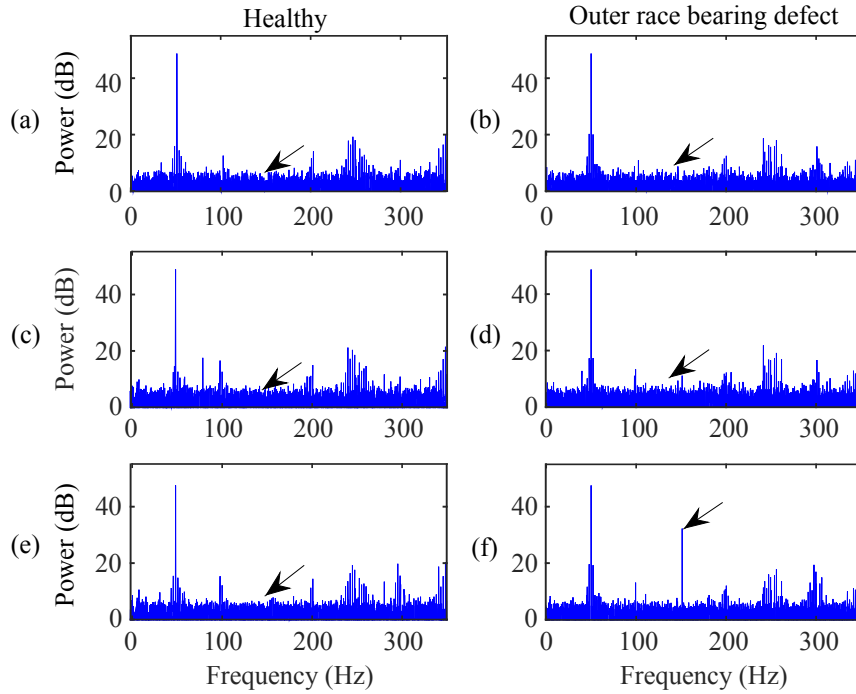
Figure 5.21. The processing results for IMs with a healthy bearing (a,c,e) and a faulty bearing (b,d,f) at 50 Hz supply frequency and full load, (a, b) Hilbert based envelope analysis, (c, d) TKE technique, (e, f) Proposed GTKE technique. (Red arrows indicate the shaft speed frequency; black arrows indicate the bearing characteristic frequency).

5.3.3 Supply Frequency 60 Hz

To examine the robustness of the proposed GTKE technique under different operating conditions, the IMs will be further tested with 60 Hz supply frequency. Figure 5.22 shows the processing results using the related techniques with no load. All of these three techniques can diagnose the IM condition when it is healthy. Unfortunately, none of these techniques could not recognize the bearing fault in this case due to low SNR. The characteristic frequency components are buried in noise.
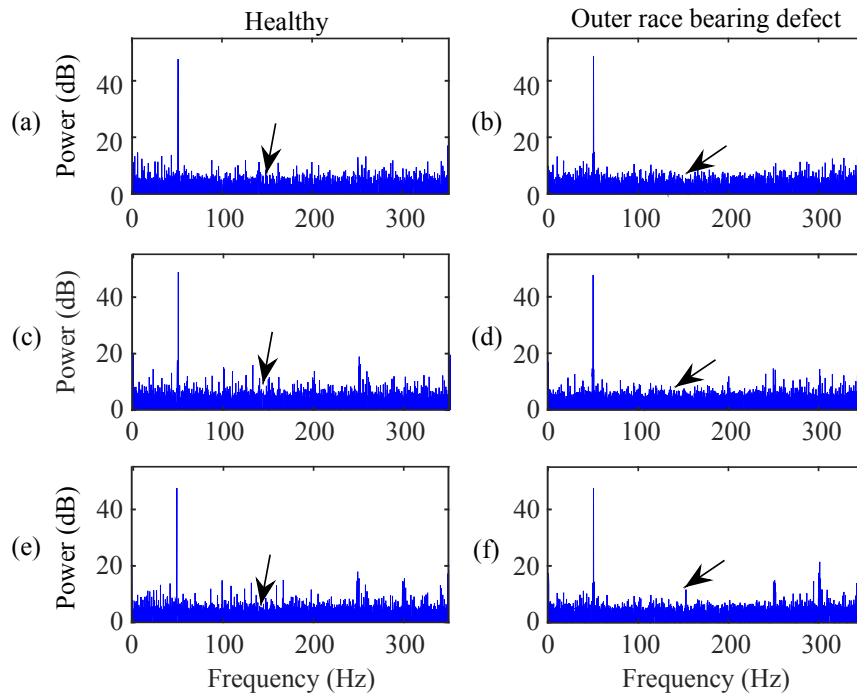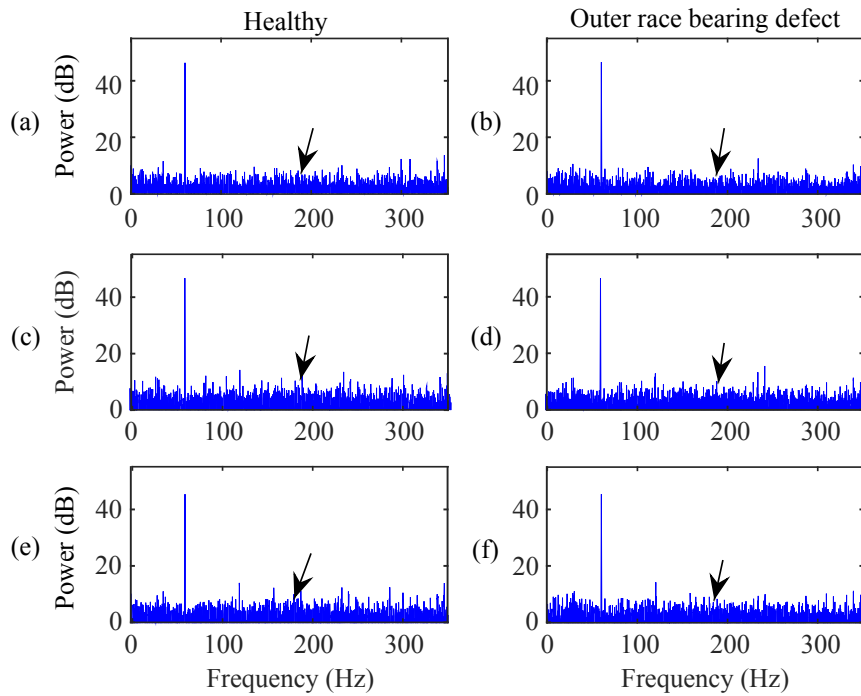
Figure 5.22. The processing results for IMs with a healthy bearing (a,c,e) and a faulty bearing (b,d,f) at 60 Hz supply frequency and no load, (a, b) Hilbert based envelope analysis, (c, d) TKE technique, (e, f) Proposed GTKE technique. (Red arrows indicate the shaft speed frequency; black arrows indicate the bearing characteristic frequency).

Similarly, when load level increases, the slip and the corresponding mechanical effects of the bearing defect become more dominant. Correspondingly, the characteristic fault frequency becomes more visible in the frequency domain representations of the tested techniques. Figure 5.23 to Figure 5.25 show the processing results of the related techniques for a healthy IM and an IM with a damaged bearing, corresponding to low, medium and heavy load conditions, respectively. It is seen that the proposed GTKE outperforms the Hilbert based envelope method and the TKE technique due to its efficiency in enhancing the spectral power of the fault related features.
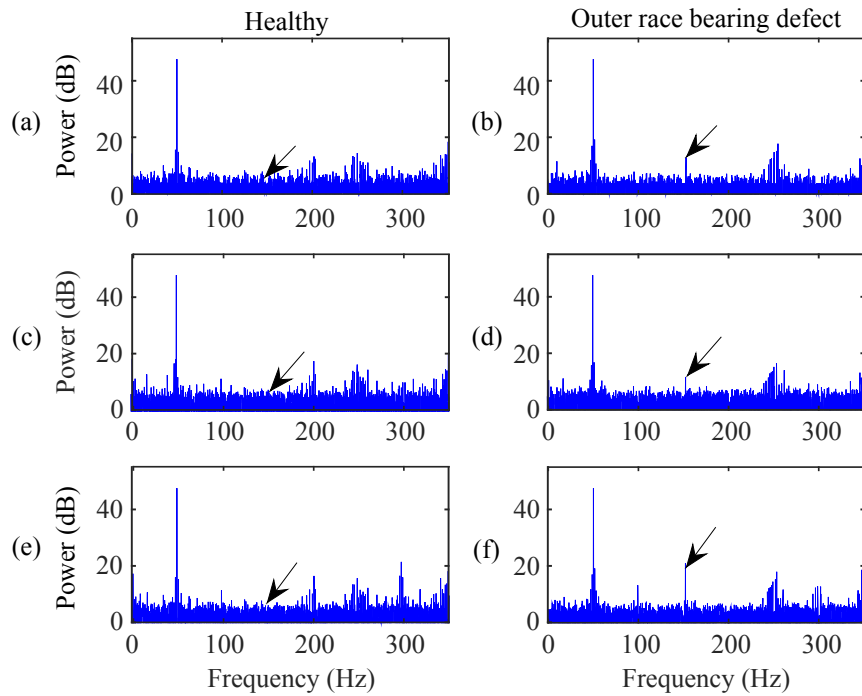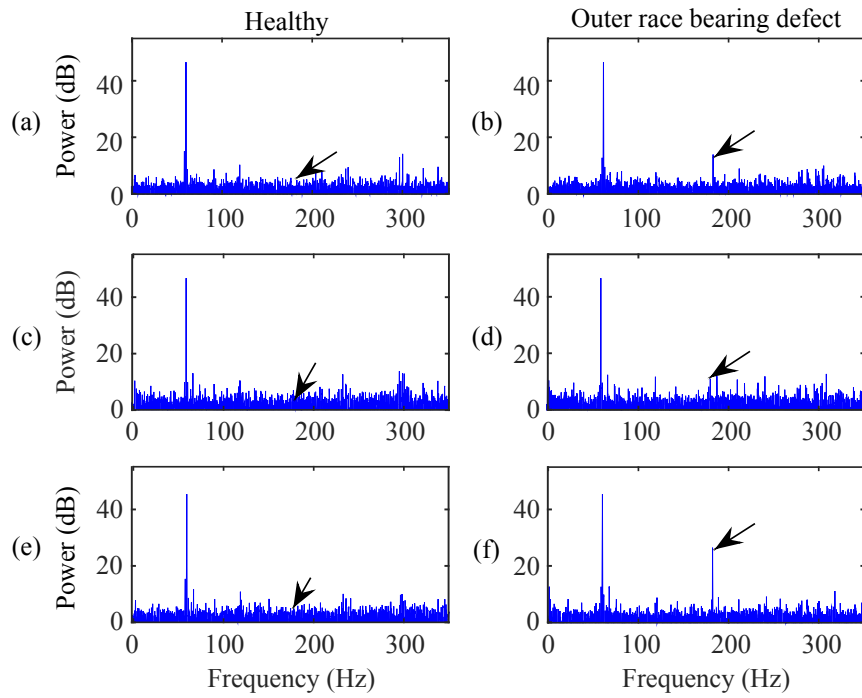
Figure 5.23. The processing results for IMs with a healthy bearing (a,c,e) and a faulty bearing (b,d,f) at 60 Hz supply frequency and low load, (a, b) Hilbert based envelope analysis, (c, d) TKE technique, (e, f) Proposed GTKE technique. (Red arrows indicate the shaft speed frequency; black arrows indicate the bearing characteristic frequency).
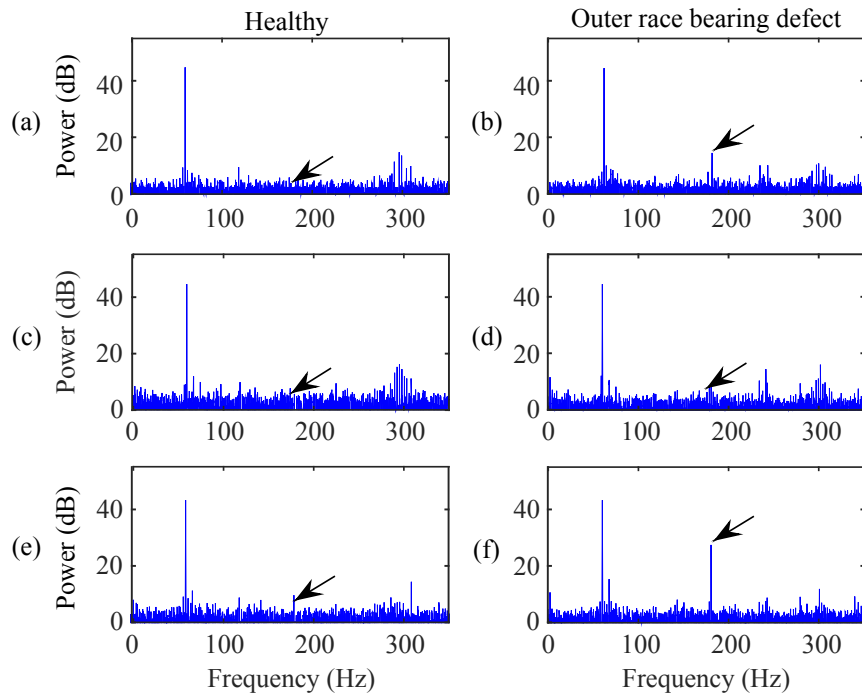
Figure 5.24. The processing results for IMs with a healthy bearing (a,c,e) and a faulty bearing (b,d,f) at 60 Hz supply frequency and medium load, (a, b) Hilbert based envelope analysis, (c, d) TKE technique, (e, f) Proposed GTKE technique. (Red arrows indicate the shaft speed frequency; black arrows indicate the bearing characteristic frequency).
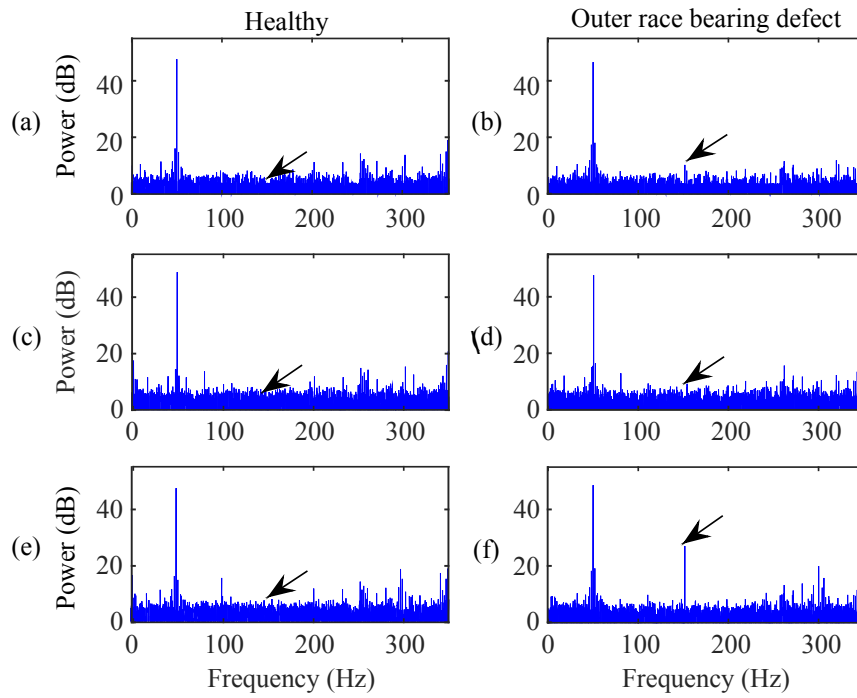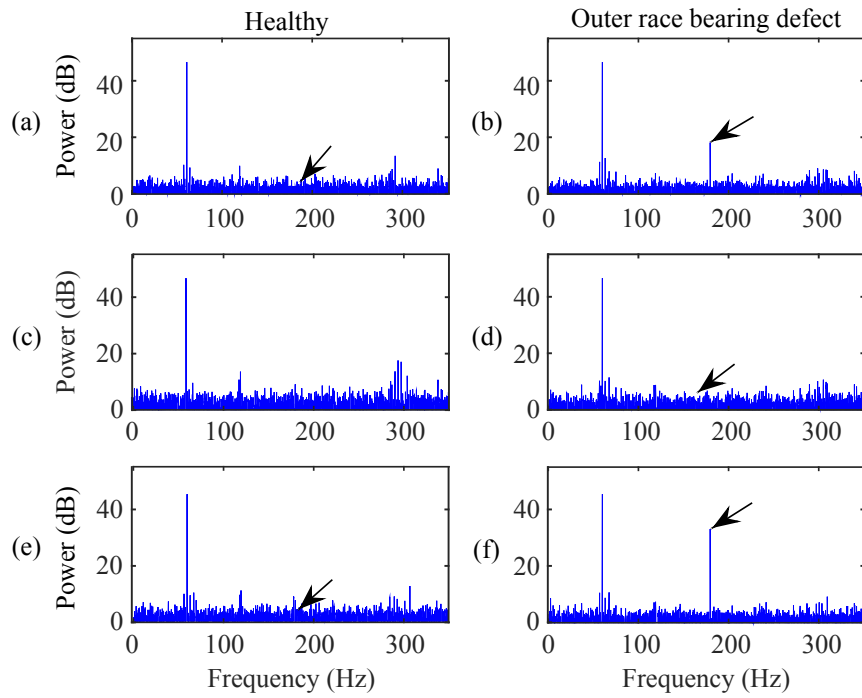
Figure 5.25. The processing results for IMs with a healthy bearing (a,c,e) and a faulty bearing (b,d,f) at 60 Hz supply frequency and full load, (a, b) Hilbert based envelope analysis, (c, d) TKE technique, (e, f) Proposed GTKE technique. (Red arrows indicate the shaft speed frequency; black arrows indicate the bearing characteristic frequency).

Chapter 6 Conclusions

6.1 Conclusions

IMs are commonly used in industrial and domestic applications. A reliable CM system for IM health diagnostics is very useful to recognize IM defects at their early stages so as to prevent the related driving machinery performance degradation and malfunction. The objective of this research is to develop a new wireless CM solution and a new technique for IM bearing fault detection.

A prototype a MCU-based smart sensor system has been developed for data acquisition. The general capability of Atmega 328p MCU has been investigated to develop an efficient ADC for data sampling and data storage. A SPI communication protocol is programmed and implemented to extend the data memory of the MCU using an additional SRAM. The ADC timing is controlled using the MCU timer and interrupt modules. A receiver-based handshake protocol is developed and primarily tested to prevent data loss in wireless transmissions. The power consumption of the MCU is studied for battery power saving in the WSS sensor node. A primary interface is designed to control the WSS system and data collection operations.

Secondly, a generalized TKE, or GTKE, technique is proposed to improve the signal-to-noise and for bearing fault. The GTKE technique uses simulated AM signals for signal demodulation. A new method is proposed to optimize lag in the GTKE to recognize the weak modulation frequencies in noisy signals. Its purpose is to improve the SNR and detect the initial outer race bearing faults in IMs that generate weak fault related signals.

A series of IM tests have been conducted to verify the effectiveness of the proposed GTKE technique for bearing fault detection, using both vibration and stator current signals (using a conventional DAQ system with higher ADC capability). Its robustness is verified by testing the IMs under different load and supply frequency supply frequency conditions. The results indicate that the GTKE technique can effectively detect the IM bearing defect using both vibration and current signals. It outperforms the related techniques in most of these test conditions.

6.2 Contributions of This Study

The following contributions have been made through the course of this study:

- An MCU software package has been developed for a WSS system with low power consumption, reliable wireless data collect.

- An adaptive interface has been developed to control the WSS operations. The functions of these related WSS modules have been verified using a WSS system.

- The GTKE technique have been implemented for fault detection.

- The lag of GTKE technique is optimized to increase the effectiveness of the technique in vibration/current signal demodulation.

6.3 Future Work

The following summarizes the future work related to this thesis project:

- Multiple SRAM ICs will be implemented to test the WSS system for online CM. The WSS system will be used to collect sufficient number of vibration/current data from the IM and will be tested for outer race bearing fault detection.

- The adaptive interface will be improved to include adjustable the sampling frequency and number of data points, to display real-time data and battery state.

- To improve the effectiveness of the TKE calculation, a signal decomposition method such as the empirical mode decomposition will be investigated to represent the original signal in terms of its monocomponent parts. Correspondingly, the GTKE technique will be tested on an IM with an inner race bearing defect and multiple faults.

References

[1] R. Isermann, Fault-Diagnosis Systems, an introduction from fault detection to fault tolerance, Darmstadt: Springer-Verlag Berlin Heidelberg, 2006.

[2] V. C. Gungor and B. Lu, and G. P. Hancke, "Opportunities and challenges of wireless sensor networks in smart grid," *IEEE Transactions on Industrial Electronics,* vol. 57, no. 10, pp. 3557-3565, 2010.

[3] S. Bandyopadhyay, and E. J. Coyle, "An energy efficient hierarchical clustering algorithm for wireless sensor networks," in *INFOCOM 2003. Twenty-Second Annual Joint Conference of the IEEE Computer and Communications. IEEE Societies*, San Francisco, 2003.

[4] W. T. Thomson, and M. Fenger, "Current signature analysis to detect induction motor faults," *IEEE Industry Applications Magazine,* vol. 1, pp. 26-34, 2001.

[5] B. Lu, B. Durocher, and P. Stemper, "Predictive maintenance techniques," *IEEE Industrial Applications Magazine,* vol. 15, no. 6, pp. 52-60, 2009.

[6] A. H. Bonnett, and G. C. Soukup, "Cause and analysis of stator and rotor failures in three-phase squirrel-cage induction motors," *IEEE Transactions on Industry Applications,* vol. 28, no. 4, pp. 921-937, 1992.

[7] S. Nandi, H. A. Toliyat, and X. Li, "Condition monitoring and fault diagnosis of electrical motors - a review," *IEEE Transactions on Energy Conversions,* vol. 20, no. 4, pp. 719-730, 2005.

[8] P. O. Donnel, "Report of large motor reliability survey of industrial and commercial installations, part I and II," *IEEE Transactions on Industial Applications,* vol. 21, no. 4, pp. 853-872, 1985.

[9] O. V. Thorsen, and M. Dalva, "A survey of faults on induction motors in offshore oil industry, petrochemical industry, gas terminals and oil refineries," *IEEE Transactions on Industrial Applications,* vol. 31, no. 5, pp. 1186-1196, 1995.

[10] S. Osman, and W. Wang, "A morphological Hilbert-Huang transform technique for bearing fault detection," *IEEE Transactions on Instrumentation and Measurement,* vol. 65, no. 11, pp. 2646-2657, 2016.

[11] Z. Kiral, and H. Karagulle, "Simulation and analysis of vibration signals generated by rollng element bearing with defects," *Tribology International,* vol. 36, no. 9, pp. 667-678, 2003.

[12] "Test & Measurement Tips, An EE World Online Resource," [Online]. Available: https://www.testandmeasurementtips.com/test-motors-oscilloscope/. [Accessed 5 March 2018].

[13] F. Immovilli, and M. Cocconelli, A. Bellini and R. Rubini, "Detection of generalized-roughness bearing fault by spectral-kurtosis energy of vibration or current signals," *IEEE Transactions on Industrial Electronics,* vol. 56, no. 11, pp. 4710-4717, 2009.

[14] R. B. Randall, Vibration-based Condition Monitoring, West Sussex: John Wiley and Sons, Ltd., 2011.

[15] G. C. M. Meijer, Smart Sensor Systems, Chichester: John Wiley & Sons, Ltd, 2008.

[16] W. Wang, and O. A. Jianu, "A smart sensing unit for vibration measurement and monitoring," *IEEE/ASME Transactions on Mechatronics,* vol. 15, no. 1, pp. 70-79, 2010.

[17] S. Middelhoek, and A. C. Hoogerwerf, "Smart sensors: when and where?," *Sensors and Actuators,* vol. 8, no. 1, pp. 39-48, 1985.

[18] B. Lu, and V. C. Gungor, "Online and remote motor energy monitoring and fault diagnostics using wireless sensor networks," *IEEE Transactions on Industrial Electronics,* vol. 56, no. 11, pp. 4651-4660, 209.

[19] R. P. Areny, and J. G. Webster, Sensors and Signal Conditioning, John Wiley & Sons, 2012.

[20] C. H. Chen, M. Y. Lin, and C. C. Liu, "Edge computing gateway of the industrial internet of things using multiple collaborative microcontrollers," *IEEE Network,* vol. 32, no. 1, pp. 24-32, 2018.

[21] X. J. Li, and G. C. M. Meijer, "A novel smart resistive-capacitive position sensor," *IEEE Transactions on Instrumentation and Measurement,* vol. 44, pp. 768-770, 1995.

[22] L. Hou, and N.W.Bergmann, "Novel industrial wireles sensor networks for machine condition monitoring and fault diagnosis," *IEEE Transactions on Instrumentation and Measurement,* vol. 61, no. 10, pp. 2787-2799, 2012.

[23] "Schaeffler Germany," [Online]. Available: https://www.schaeffler.de/content.schaeffler.de/en/products-and-solutions/industrial/produktportfolio/index.jsp?app=portfolio&filtertype=categories&categ ories=Rolling%20bearings%20and%20plain%20bearings%2CBall%20bearings. [Accessed 15 03 2018].

[24] W. Zhou, T. G. Habetler, and R. G. Harley, "Stator current-based bearing fault detection techniques: A general review," in *IEEE International Symposium on Diagnostics for Electric Machines, Power Electronics and Drives,* , Cracow, 2007.

[25] P. D. McFadden, and J. D. Smith, "Model for the vibration produced by a single point defect in a rolling element bearing," *Journal of Sound and Vibration,* vol. 96, no. 1, pp. 69-82, 1983.

[26] Y. T. Su, and S. J. Lin, "On initial fault detection of a tapered roller bearing: Frequency domain analysis," *Journal of Sound and Vibration,* vol. 155, no. 1, pp. 75-84, 1992.

[27] S. Osman, and W. Wang, "A normalized Hilbert-Huang transform technique for bearing fault detection," *Journal of Vibration and Control,* vol. 22, no. 11, pp. 2771-2787, 2016.

[28] J. Liu, W. Wang, and F. Ma, "Bearing system health condition monitoring using a wavelet cross-spectrum analysis technique," *Journal of Vibration and Control,* vol. 18, pp. 953-963, 2001.

[29] R. Rubini, and U. Meneghetti, "Application of the envelope and wavelet transform analysis for the diagnosis of incipient faults in ball bearings," *Mechanical Systems and Signal Processing,* vol. 15, no. 2, pp. 287-302, 2001.

[30] Q. Du, and S. Yang, "Application of the EMD method in vibration analysis of ball bearings," *Mechanical Systems and Signal Prcessing,* vol. 21, no. 6, pp. 2634-2644, 2007.

[31] W. A. Smith, and R. B. Randall, "Rolling element bearing diagnostics using the Case Western Reserve university data: a benchmark study," *Mechanical systems and signal processing,* vol. 64, pp. 100-131, 2015.

[32] N. Sawalhi, and R. B. Randall, "Vibration response of spalled rolling element bearings: Observations, simulations and signal processing techniques to track the spall size," *Mechanical Systems and Signal Processing,* vol. 25, no. 3, pp. 847-870, 2011.

[33] J. Antoni, and R.B. Randall, "The spectral kurtosis: application to the vibratory surveillance and diagnostics of rotating machines," *Mechanical Systems and Signal Processing,* vol. 20, no. 2, pp. 308-331, 2006.

[34] R. B. Randall, and J. Antoni, "Rolling element bearing diagnostics - A tutorial," *Mechanical Systems and Signal Processing,* vol. 25, no. 2, pp. 485-520, 2011.

[35] P. H. Rodriguez, J. B. Alonso, M. A. Ferrer, and C. M. Travieso, "Application of the Teager-Kaiser energy operator in bearing fault diagnosis," *ISA Transactions,* vol. 52, no. 2, pp. 278-284, 2013.

[36] H. Li, Y. Zhang, and H. Zheng, "Bearing fault detection and diagnosis based on order tracking and Teager-Huang Transform," *Journal of Mechanical Science,* vol. 25, no. 3, pp. 811-822, 2010.

[37] Z. Feng, M. J. Zuo, R. Hao, F. Chu, and J. Lee, "Ensemble empirical mode decomposition based Teager energy spectrum for bearing fault diagnosis," *Journal of Vibration and Acoustics,* vol. 135, no. 3, pp. 031013 - 1-21, 2013.

[38] D. J. Linehan, S. L. Bunch, and B. B. Hanzelka, "Cost-effective on-line monitoring of rotating equipment using motor current analysis," Vibration Institute, Virginia Beach, 1990.

[39] B. Samatnta, K. R. A. Balushi, and S. A. A. Araimi, "Artificial neural networks and support vector machines with genetic algorith for bearing fault detection," *Engineering Applications of Artificial Intelligence,* vol. 16, no. 7-8, pp. 653-665, 2003.

[40] M. E. H. Benbouzid, "A review of induction motors signature analysis as a medium of faults detection," *IEEE Transactions on Industrial Applications,* vol. 47, no. 5, pp. 984-993, 2000.

[41] R. R. Schoen, T. G. Habetler, F. Kamran, and R. G. Bartheld, "Motor bearing damage detection using stator current monitoring," *IEEE Transactions on Industrial Applications,* vol. 31, no. 6, pp. 1274-1279, 1995.

[42] M. Blodt, P. Granjon, B. Raison, and G. Rostaing, "Models for bearing damage detection in induction motors using stator current modelling," *IEEE Transactions on Industrial Applications,* vol. 55, no. 4, pp. 1813-1822, 2008.

[43] E. C. C. Lau, H. W. Ngan, "Detection of motor bearing outer raceway defect by wavelet packet transformed motor current signature analysis," *IEEE Transactions on instrumentation and measurement,* vol. 59, no. 10, pp. 2683-2691, 2010.

[44] A. Soualhi, K. Medjaher, and N. Zerhouni, "Bearing health monitoring based on Hilbert-Huang transform, support vector machine, and regression," *IEEE Transactions on Instrumentation and Measurement,* vol. 64, no. 1, pp. 52-63, 2015.

[45] F. Immovilli, C. Bianchini, M. Cocconcelli, A. Bellini, and R. Rubini, "Bearing fault model for induction motor with externally induced vibration," *IEEE Transactions on Industrial Electronics,* vol. 60, no. 8, pp. 3408-3419, 2013.

[46] E. H. E. Bouchikhi, V. Choqueuse, and M. E. H. Benbouzid, "Current frequency spectral subtraction and its contribution to induction machines' bearings condition monitoring," *IEEE Transactions on Energy Conversion,* vol. 28, no. 1, pp. 135-145, 2013.

[47] K. Bacha, S. B. Salem, and A. Caari, "An improved combination of Hilbert and Park transforms for fault detection and identification in three-phase induction motors," *International Journal of Electical Power and Energy Systems,* vol. 43, no. 1, pp. 1006-1016, 2012.

[48] D. Z. Li, W. Wang, and F. Ismail, "A spectrum synch technique for induction motor health condition monitoring," *IEEE Transactions on Energy Conversion,* vol. 30, no. 4, pp. 1348-1356, 2015.

[49] M. Blodt, D. Bonacci, M. Chabert, and J Faucher, "On-line monitoring of mechanical faults in variable-speed induction motor drives using the Wigner distribution," *IEEE Transactions on Industrial Electronics,* vol. 55, no. 2, pp. 522-533, 2008.

[50] W. Zhou, T. G. Habetler, and R. G. Harley, "Bearing fault detection via stator current noise cancellation and statistical control," *IEEE Transactions on Industrial Electronics,* vol. 55, no. 12, pp. 4260-4269, 2008.

[51] F. Dalvand, S. Dalvand, F. Sharafi, and M. Pecth, "Current noise cancellation for bearing fault diagnostics using time shifting," *IEEE Transactions on Industrial Electronics,* vol. 64, no. 10, pp. 8138-8147, 2017.

[52] J. Zarei, and J. Poshtan, "Bearing fault detection using wavelet packet transform of induction motor stator current," *Tribology International,* vol. 40, no. 5, pp. 763-769, 2007.

[53] A. Bellini, F. Immovilli, R. Rubini, and C. Tassoni, "Diagnosis of bearing faults of induction machines by vibration or current signals: A critical comparison," *IEEE Transactions on Industrial Applications,* vol. 46, no. 4, pp. 1350-1359, 2010.

[54] "Current Transducer LTS 6-NP," LEM, 2017.

[55] "Direct Industry," [Online]. Available: http://www.directindustry.com/prod/shenzhen-socan-technologies-co-ltd/product-132598-1671412.html. [Accessed 29 May 2018].

[56] S. Barrett, Embedded systems design with Atmel AVR microcontroller, part I, Morgan & Claypool Publishers, 2009.

[57] J. M. Rabaey, A. Chandrakasan, and B. Nikolic, Digital integrated circuits, New Delhi: PHI Learning Private Ltd., 2011.

[58] Atmel, "8-bit AVR microcontrollers, ATmega328/P," Atmel , 2016.

[59] "IEEE standard letter designations for radar-frequency bands, IEEE Std 521," The Institute of Electrical and Electronics Engineers, New York, 1984.

[60] F. Ellinger, Radio frequency integrated circuits and technologies, Berlin: Springer, 2008.

[61] M. Blodt, M. Chabert, J. Regnier, and J. Faucher, "Mechanical load fault detection in induction motors by stator current time-frequency analysis," *IEEE Transactions on Industry Applications,* vol. 42, no. 6, pp. 1454-1464, 2006.

[62] J. Cheng, Y. Yang, and Y. Yang, "A rotating machinery fault diagnosis method based on local mean decomposition," *Digital Signal Processing,* vol. 22, no. 2, pp. 356-366, 20121.

[63] S. Haykin, and B. V. Veen, Signals and systems, New York: John Wiley & Sons, Inc., 1999.

[64] R. L. Schiltz, "Forcing frequency identification of rolling element bearings," *Sound and Vibration,* vol. 24, no. 5, pp. 16-19, 1990.

[65] V. C. M. N. Leite, J. G. B. Silva, G. F. C. Veloso, L. E. B. Silva, G. Lambert-Torres, E. L. Bonaldi, and L. E. Oliveria, "Detection of localized bearing faults in induction machines by spectral kurtosis and envelope analysis of stator current," *IEEE Transactions on Industrial Electronics,* vol. 62, no. 3, pp. 1855-1865, 2015.

[66] J. F. Kaiser, "On a simple algorithm to calculate the energy of a signal," in *Acoustics, Speech, and Signal Processing*, Albuquerque, 1990.

[67] D. Dimitriadis, A. Potamianos, and P. Maragos, "A comparison of the squared energy and Teager-Kaiser operators for short-term energy estimation in additive noise," *IEEE Transactions on Signal Processing,* vol. 57, no. 7, pp. 2569-2582, 2009.

[68] I. Kamwa, A. K. Pradhan, and G. Joos, "Robust detection and analysis of power system oscillations using the Teager-Kaiser energy operator," *IEEE Transactions on Power Systems,* vol. 26, no. 1, pp. 323-334, 2011.

[69] D. Vakman, "On the analytic signal, the Teager-Kaiser energy algorithm, and other methods for defining amplitude and frequency," *IEEE Transactions on Signal Procesing,* vol. 44, no. 4, pp. 791-798, 1996.

[70] D. Z. Li, and W. Wang, "An enhanced bispectrum technique with auxiliary frequency injection for induction motor health condition monitoring," *IEEE Transactions on Instrumentation and Measurement,* vol. 64, no. 10, pp. 2679-2687, 2015.

[71] W. Lin, C. Hamilton, and P. Chitrapu, "A generalization of the Teager-Kaiser energy functions and application to resolving two closely-spaced tones," *IEEE Signal Processing Letters,* vol. 2, no. 8, pp. 152-154, 1995.